

# JCMT HARP CO 3–2 observations of molecular outflows in W5

Adam Ginsburg,<sup>1</sup>★ John Bally<sup>1</sup> and Jonathan P. Williams<sup>2</sup>

<sup>1</sup>Center for Astrophysics and Space Astronomy, University of Colorado 389 UCB, Boulder, CO 80309-0389, USA

<sup>2</sup>Institute for Astronomy, University of Hawaii 2680 Woodlawn Dr. Honolulu, HI 96822, USA

Accepted 2011 June 16. Received 2011 June 16; in original form 2010 June 30

## ABSTRACT

New James Clerk Maxwell Telescope (JCMT) HARP CO 3–2 observations of the W5 star forming complex are presented, totalling an area of  $\sim 12\,000$  arcmin $^2$  with sensitivity better than 0.1 K per 0.4 km s $^{-1}$  channel. We discovered 55 CO outflow candidates, of which 40 are associated with W5 and 15 are more distant than the Perseus arm. Most of the outflows are located on the periphery of the W5 H II region. However, two outflow clusters are  $> 5$  pc from the ionization fronts, indicating that their driving protostars formed without directly being triggered by the O-stars in W5. We compare the derived outflow properties to those in Perseus and find that the total W5 outflow mass is surprisingly low given the cloud masses. The outflow mass deficiency in the more massive W5 cloud [ $M(\text{H}_2) \sim 5 \times 10^4 M_\odot$ ] can be explained if ionizing radiation dissociates molecules as they break out of their host cloud cores. Although CO  $J = 3-2$  is a good outflow tracer, it is likely to be a poor mass tracer because of sub-thermal line excitation and high opacity, which may also contribute to the outflow mass discrepancy. It is unlikely that outflows could provide the observed turbulent energy in the W5 molecular clouds even accounting for undetected outflow material. Many cometary globules have been observed with velocity gradients from head to tail, displaying strong interaction with the W5 H II region and exhibiting signs of triggered or revealed star formation in their heads. Because it is observed face-on, W5 is an excellent region to study feedback effects, both positive and negative, of massive stars on star formation.

**Key words:** stars: formation – ISM: individual: W5 – ISM: jets and outflows – ISM: kinematics and dynamics.

## 1 INTRODUCTION

Galactic-scale shocks such as spiral density waves promote the formation of giant molecular clouds (GMCs) where massive stars, star clusters and OB associations form. The massive stars in such groups can either disrupt the surrounding medium or promote further star formation. While ionizing and soft UV radiation, stellar winds, and eventually supernova explosions, destroy clouds in the immediate vicinity of massive stars, as the resulting bubbles age and decelerate; they can also trigger further star formation. In the ‘collect and collapse’ scenario (e.g. Elmegreen & Lada 1977), gas swept-up by expanding bubbles can collapse into new star-forming clouds. In the ‘radiation-driven implosion’ model (Klein, Sandford & Whitaker 1983; Bertoldi & McKee 1990), pre-existing clouds may be compressed by photoablation pressure or by the increased pressure as they are overrun by an expanding shell. In some circumstances, forming stars are simply exposed as low-density gas is removed by winds and radiation from massive stars. These pro-

cesses may play significant roles in determining the efficiency of star formation in clustered environments (Elmegreen 1998).

Feedback from low-mass stars may also control the shape of the stellar initial mass function in clusters (Adams & Fatuzzo 1996; Peters et al. 2010). Low-mass young stars generate high-velocity, collimated outflows that contribute to the turbulent support of a gas clump, preventing the clump from forming stars long enough that it is eventually blown away by massive star feedback. It is therefore important to understand the strength of low-mass protostellar feedback relative to other feedback mechanisms.

Outflows are a ubiquitous indicator of the presence of ongoing star formation (Reipurth & Bally 2001). CO outflows are an indicator of ongoing embedded star formation at a younger stage than optical outflows because shielding from the interstellar radiation field is required for CO to survive. Although Herbig–Haro shocks and H<sub>2</sub> knots reveal the locations of the highest-velocity segments of these outflows, CO has typically been thought of as a ‘calorimeter’ measuring the majority of the mass and momentum ejected from protostars or swept up by the ejecta (Bachiller 1996).

The W5 star forming complex in the outer galaxy is a prime location to study massive star formation and triggering. The

\*E-mail: adam.ginsburg@colorado.edu

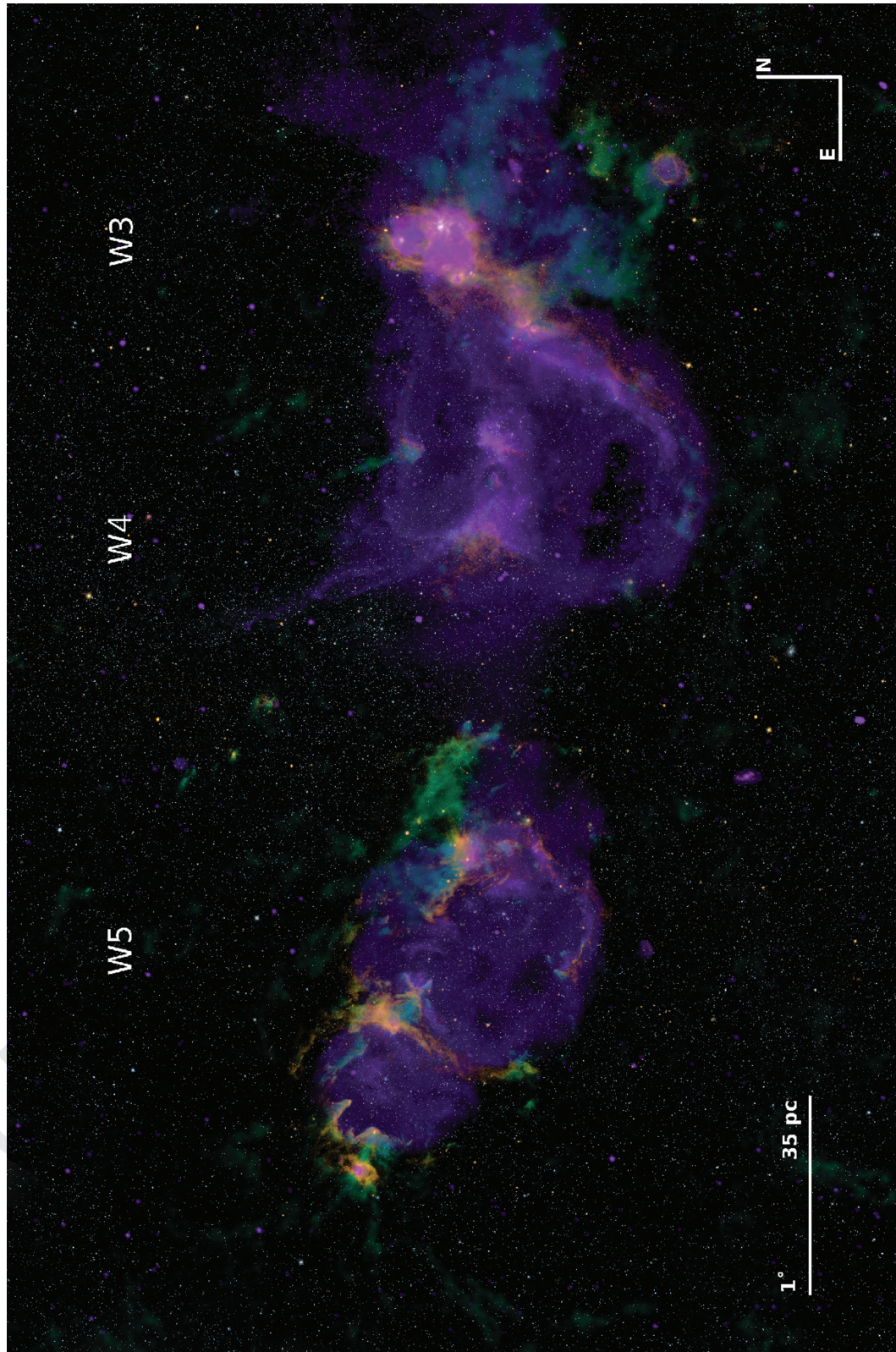


**Figure 1.** An overview of the W3/4/5 complex (also known as the ‘Heart and Soul Nebula’) in false colour. Orange shows  $8 \mu\text{m}$  emission from the *Spitzer* and *MSX* satellites. Purple shows  $21 \text{ cm}$  continuum emission from the **DRAO CGPS** (Taylor et al. 2003); the **DSS R** image was used to set the display opacity of the  $21 \text{ cm}$  continuum (purely for aesthetic purposes). The green shows JCMT  $^{12}\text{CO}$  3–2 along with FCRAO  $^{12}\text{CO}$  1–0 to fill in gaps that were not observed with the JCMT. The image spans  $\sim 7^\circ$  in galactic longitude. This overview image shows the hypothesized interaction between the W4 superbubble and the W3 and W5 star-forming regions (Oey et al. 2005).

Both the text and the symbols in the figure look blocky. In particular, some of the circles are incomplete. If you need a higher quality or different form of this figure, I can provide it.

3

Q12

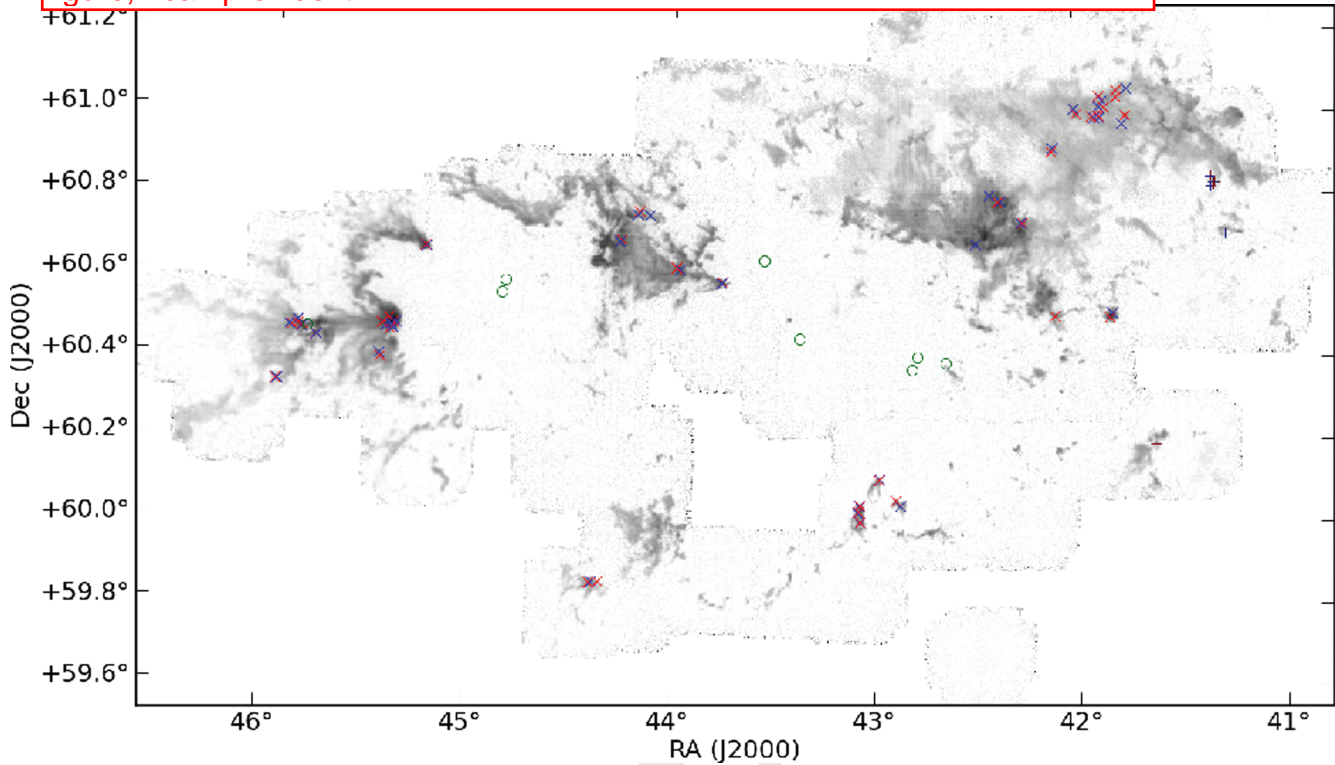


**Figure 2.** A mosaic of the CO 3–2 data cube integrated from  $-20$  to  $-60$   $\text{km s}^{-1}$ . The grey-scale is linear from 0 to  $150 \text{ K km s}^{-1}$ . The red and blue Xs mark the locations of redshifted and blueshifted outflows. Dark red and dark blue plus symbols mark outflows at outer-arm velocities. Green circles mark the location of all known B0 and earlier stars in the W5 region from SIMBAD.

Q13

bright-rimmed clouds in W5 have been recognized as good candidates for ongoing triggering by a number of groups (Lefloch, Lazareff & Castets 1997; Karr & Martin 2003; Thompson et al. 2004). The clustering properties were analysed by Koenig et al. (2008) using *Spitzer* infrared data, and a number of significant clusters were discovered. The whole W5 complex may be a product of triggering, as it is located on one side of the W4 chimney thought to be created by multiple supernovae during the last  $\sim 10$  Myr (Oey et al. 2005, Fig. 1).

Following Koenig et al. (2008), we adopt a distance to W5 of 2 kpc based on the water-maser parallax distance to the neighbouring W3(OH) region (Hachisuka et al. 2006). As with W3, the W5 cloud is substantially ( $\approx 1.5 \times$ ) closer than its kinematic distance would suggest [ $v_{\text{LSR}}(-40 \text{ km s}^{-1}) \approx 3 \text{ kpc}$ ]. Given this distance, Koenig et al. (2008) derived a total gas mass of  $6.5 \times 10^4 \text{ M}_\odot$  from a  $2 \mu\text{m}$  extinction map.

The W5 complex was mapped in the  $^{12}\text{CO}$  1–0 emission line by the Five College Radio Astronomy Observatory (FCRAO) using the **SEQUOIA** receiver array (Heyer et al. 1998). The same array was used to map W5 in the  $^{13}\text{CO}$  1–0 line (C. Brunt, private communication). Some early work searched for outflows in W5 (Bretherton, Moore & Ridge 2002), but the low-resolution CO 1–0 data only revealed a few, and only one was published. The higher resolution and sensitivity observations presented here reveal many additional outflows.

While W5 is thought to be associated with the W3/4/5 complex, there are other infrared sources in the same part of the sky that are not obviously associated with W5. Some of these have been noted to be in the outer arm (several kpc behind W5) by Digel et al. (1996) and Snell, Carpenter & Heyer (2002).

In Section 2, we present the new and archival data used in our study. In Section 3, we discuss the outflow detection process and compare outflow detectability in W5 to that in Perseus. In Section 4, we discuss the physical properties of the outflows and their implications for star formation in the W5 complex. In Section 5, we briefly describe the outer-arm outflows discovered.

## 2 OBSERVATIONS

### 2.1 JCMT HARP CO 3–2

CO  $J = 3-2$  345.79599 GHz data were acquired at the 15-m James Clerk Maxwell Telescope (JCMT) using the HARP array on a series of observing runs in 2008. On 2008 January 2–4,  $\sim 800 \text{ arcmin}^2$  were mapped. During the run,  $\tau_{225}$ , the zenith opacity at 225 GHz measured using the Caltech Submillimetre Observatory tipping radiometer ranged from 0.1 to 0.4 ( $0.4 < \tau_{345 \text{ GHz}} < 1.6^1$ ). Additional areas were mapped on August 4–7, October 16–20 and 31, and 2008 November 1 and 12–15 in similar conditions. A total of  $\sim 3 \text{ deg}^2$  ( $12\,000 \text{ arcmin}^2$ ) in the W5 complex were mapped (a velocity-integrated mosaic is shown in Fig. 2).

HARP is a 16 pixel SIS receiver array acting as a front-end to the ACSIS digital auto-correlation spectrometer. In 2008 January, 14 of the 16 detectors were functional. In the second half of 2008, 12 of 16 were functional, necessitating longer scans to achieve similar signal-to-noise ratio (S/N).

Q14

Q15

<sup>1</sup> <http://docs.jach.hawaii.edu/JCMT/SCD/SN/002.2/node5.html>

In 2008 January, a single spectral window centred at 345.795 9899 with bandwidth 1.0 GHz and channel width 488 kHz ( $0.42 \text{ km s}^{-1}$ ) was used. In 2008 August and later, we used 250 MHz bandwidth and 61 kHz ( $0.05 \text{ km s}^{-1}$ ) channel width. At this frequency, the beam full width at half-maximum (FWHM) is 14 arcsec (0.14 pc at a distance of 2 kpc).<sup>2</sup>

A raster mapping strategy was used. In 2008, the array was shifted by 1/2 of an array spacing (58.2 arcsec) between scans. Data were sampled at a rate of 0.6 s per integration. Two perpendicular scans were used for each field observed. Most fields were  $10 \times 10$  arcmin and took  $\sim 45$  min. When only 12 receptors were available, 1/4 array stepping (29.1 arcsec) was used with a sample rate of 0.4 s per integration.

Data were reduced using the **SMURF** package within the STARLINK software distribution.<sup>3</sup> The **SMURF** command **MAKECUBE** was used to generate mosaics of contiguous sub-fields. The data were gridded onto cubes with 6 arcsec pixels and smoothed with a  $\sigma = 2$ -pixel Gaussian, resulting in a map FWHM resolution of 18 arcsec (0.17 pc). A linear fit was subtracted from each spectrum over emission-free velocities (generally  $-60$  to  $-50$  and  $-20$  to  $-10 \text{ km s}^{-1}$ ) to remove the baseline. The final map rms was  $\sigma_{T_A^*} \sim 0.06\text{--}0.11 \text{ K}$  in  $0.42 \text{ km s}^{-1}$  channels.

The sky reference position (off position) in 2008 January was J2000 2:31:04.069 +62:59:13.81. In later epochs, off positions closer to the target fields were selected from blank sky regions identified in 2008 January in order to increase observing efficiency. A main-beam efficiency  $\eta_{\text{mb}} = 0.60$  was used as per the JCMT website to convert measurements to  $T_{\text{mb}}$ , though maps and spectra are presented in the original  $T_A^*$  units.

## 2.2 FCRAO Outer Galaxy Survey

The FCRAO Outer Galaxy Survey (OGS) observed the W5 complex in  $^{12}\text{CO}$  (Heyer et al. 1998) and  $^{13}\text{CO}$  1–0 (C. Brunt, private communication). The  $^{13}\text{CO}$  data cube achieved a mean sensitivity of  $0.35 \text{ K}$  per  $0.13 \text{ km s}^{-1}$  channel, or  $0.6 \text{ K km s}^{-1}$  integrated. The  $^{13}\text{CO}$  cube was integrated over all velocities and resampled to match the **BGPS** map using the **MONTAGE**<sup>4</sup> package. The FWHM beam size was  $\theta_B = 50.0$  arcsec (0.48 pc). The integrated  $^{12}\text{CO}$  data cube, with a sensitivity  $\sigma = 1 \text{ K km s}^{-1}$ , is displayed with region name identifications in Fig. 3.

## 2.3 Spitzer

**Spitzer** IRAC and MIPS 24  $\mu\text{m}$  images from Koenig et al. (2008) were used for morphological comparison. The reduction and extraction techniques are detailed in their paper.

## 3 ANALYSIS

### 3.1 Outflow detections

Outflows were identified in the CO data cubes by manually searching through position–velocity space for line wings using STARLINK’s **GAIA** display software. Outflow candidates were identified by high-velocity wings inconsistent with the local cloud velocity distribution, which ranged from a width of  $3 \text{ km s}^{-1}$  to  $7 \text{ km s}^{-1}$ . Once an

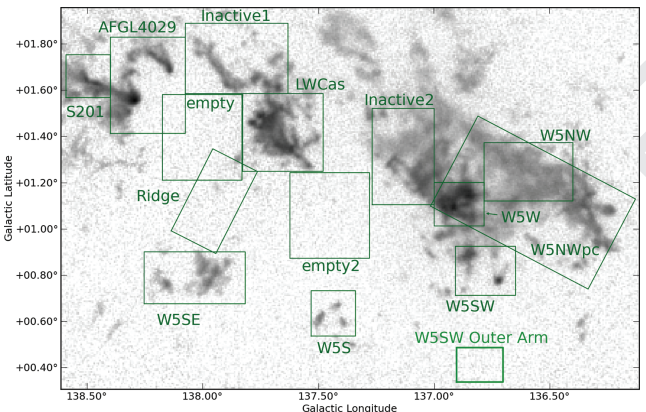


**Figure 3.** Individual region masks overlaid on the FCRAO  $^{12}\text{CO}$  integrated image. The named regions, S201, AFGL 4029, LWCas, W5NW, W5W, W5SE, W5S and W5SW, were all selected based on the presence of outflows within the box. The inactive regions were selected from regions with substantial CO emission but without outflows. The ‘empty’ regions have essentially no CO emission within them and are used to place limits on the molecular gas within the east and west ‘bubbles’. W5NWpc is compared directly to the Perseus molecular cloud in Section 3.1.1.

outflow candidate was identified in the position–velocity diagrams, the velocity range over which the wing showed emission in the position–velocity diagram (down to  $T_A^* = 0$ ) was integrated over to create a map from which the approximate outflow size and position were determined (e.g. Figs 4 and 5).

Unlike Curtis et al. (2010) and Hatchell & Dunham (2009), we did not use an ‘objective’ outflow identification method because of the greater velocity complexity and poorer spatial resolution of our observations. The outflow selection criteria in these papers require the presence of a sub-mm clump in order to identify a candidate driving source (and therefore a targeted region in which to search for outflows), making a similar objective identification impossible for our survey. As discussed later in Section 4, the regions associated with outflows have wide lines and many are double-peaked. Additionally, many smaller areas associated with outflows have collections of Gaussian-profiled clumps that are not connected to the cloud in position–velocity diagrams but are not outflows. In particular, W5 is pockmarked by dozens of small cometary globules that are sometimes spatially coincident with the clouds but slightly offset in velocity.

While Arce et al. (2010) described the benefits of 3D visualization using isosurface contours, we found that the varying S/N across large-scale ( $\sim 500 \text{ pixel}^2$ ) regions with significant extent in RA/Dec. and a limited velocity dynamic range made this method difficult for W5. There were many low-intensity outflows that were detectable by careful searches through position–velocity space that are not as apparent using isosurface methods. Out of the 55 outflows reported here, only 14<sup>5</sup> would be considered obvious, high-intensity, high-velocity flows from their spectra alone; the rest could not be unambiguously detected without a search through position–velocity space.

In the majority of sources, the individual outflow lobes were unresolved, although some showed hints of position–velocity gradients at low significance and in many the red and blue flows are spatially separated. Only Outflow 1’s lobes were clearly resolved

<sup>2</sup> [http://docs.jach.hawaii.edu/JCMT/OVERVIEW/tel\\_overview/](http://docs.jach.hawaii.edu/JCMT/OVERVIEW/tel_overview/)

<sup>3</sup> <http://starlink.jach.hawaii.edu/>

<sup>4</sup> <http://montage.ipac.caltech.edu/>

<sup>5</sup> Outflows 15, 20, 24, the cluster of outflows 26–32, 47, 48, 52 and 53 could all have readily been detected by pointed single-dish measurements.

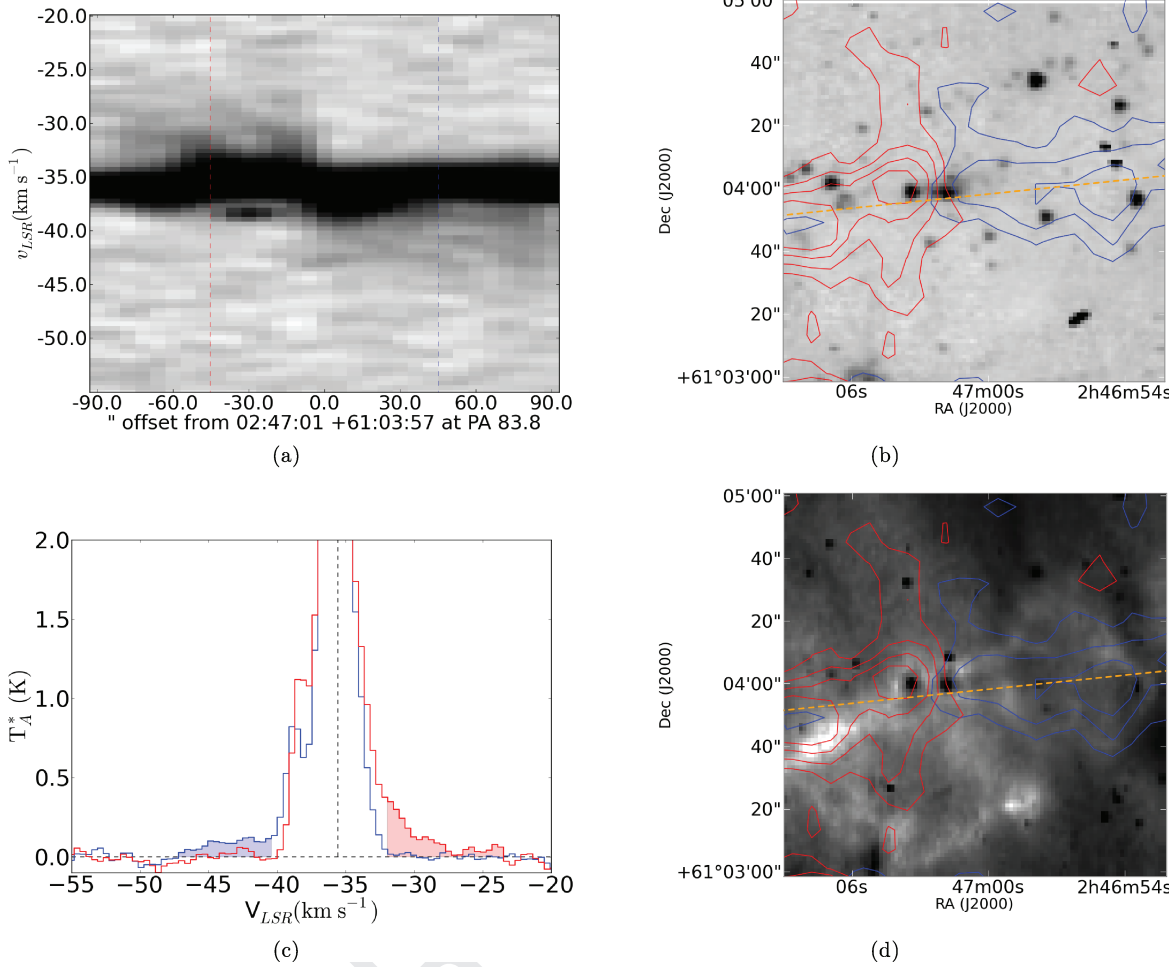


**Figure 4.** Position–velocity diagrams (a), spectra (c) and contour overlays of Outflow 1 on  $Spitzer$  4.5  $\mu m$  (b) and 8  $\mu m$  (d) images. This outflow is clearly resolved and bipolar. (a) Position–velocity diagram of the blue flow displayed in arcsinh stretch from  $T_A^* = 0$  to 3 K. Locations of the red and blue flows are indicated by vertical dashed lines. The location of the position–velocity cut is indicated by the orange dashed line in panels (b) and (d), although the position–velocity cut is longer than those cut-out images. (b)  $Spitzer$  4.5  $\mu m$  image displayed in logarithmic stretch from 30 to 500 MJy sr $^{-1}$ . (c) Spectrum of the outflow integrated over the outflow aperture and the velocity range specified with shading. The velocity centre (vertical dashed line) is determined by fitting a Gaussian to the  $^{13}\text{CO}$  spectrum in an aperture including both outflow lobes. In the few cases in which  $^{13}\text{CO}$  1–0 was unavailable, a Gaussian was fit to the  $^{12}\text{CO}$  3–2 spectrum. (d) Contours of the red and blue outflows superposed on the  $Spitzer$  8  $\mu m$  image displayed in logarithmic stretch. The contours are generated from a total intensity image integrated over the outflow velocities indicated in panel (c). The contours in both panels (b) and (d) are displayed at levels of 0.5, 1, 1.5, 2, 3, 4, 5, 6 K km s $^{-1}$  ( $\sigma \approx 0.25$  K km s $^{-1}$ ). The contour levels and stretches specified in this caption apply to all of the figures in the supplementary materials except where otherwise noted.

(Fig. 4). Some of most suggestive gradients occurred where the outflow merged with its host molecular cloud in position–velocity space, making the gradient difficult to distinguish (e.g. Outflow 12; Fig. 6). Bipolar pairs were selected when there were red and blue flows close to one another. The classification of a bipolar flow was either ‘yc’ (yes – confident), ‘yu’ (yes – unconfident) or ‘n’ (no) in Table 2. This identification is discussed in the captions for each outflow figure in the Supporting Information with the online version of the article. The AFGL 4029 region has many red and blue lobes but confusion prevented pairing.

In cases where only the red- or blueshifted lobe was visible, the surrounding pixels were searched for lower-significance and lower-velocity counterparts. For cases in which emission was detected, a candidate counterflow was identified and incorporated into the catalogue. However, in 12 cases, the counterflow still evaded detection, either because of confusion or because the counterflow is not present in CO.

The outflow positions are overlaid on the CO 3–2 image in Fig. 2 to provide an overview of where star formation is most active. The figures in Section 5.2 show outflow locations overlaid on small-scale images.

Because our detection method involved searching for high-velocity outflows by eye, there should be no false detections. However, it is possible that some of these outflows are generated by mechanisms other than protostellar jets and winds since we have not identified their driving sources.

One possible alternative driving mechanism is a photoevaporation flow, which could be accelerated up to the sound speed of the ionized medium,  $c_{\text{II}} \approx 10$  km s $^{-1}$ . Gas accelerating away from the cloud would not be detected as an outflow because it would be rapidly ionized. However, gas driven inward would be accelerated and remain molecular. It could exhibit red and/or blue flows depending on the line-of-sight orientation. While there are viable candidates for this form of outflow impersonator, such flows can

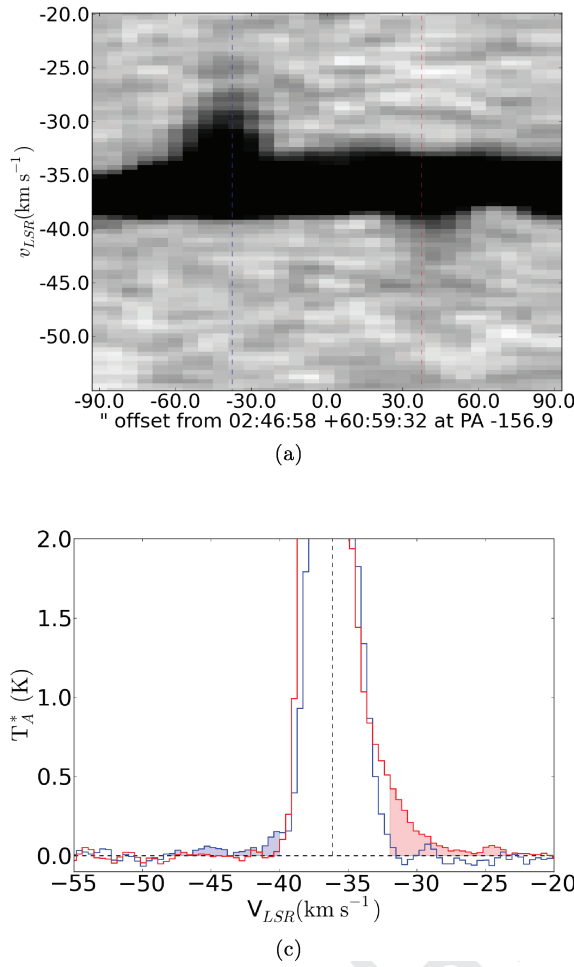


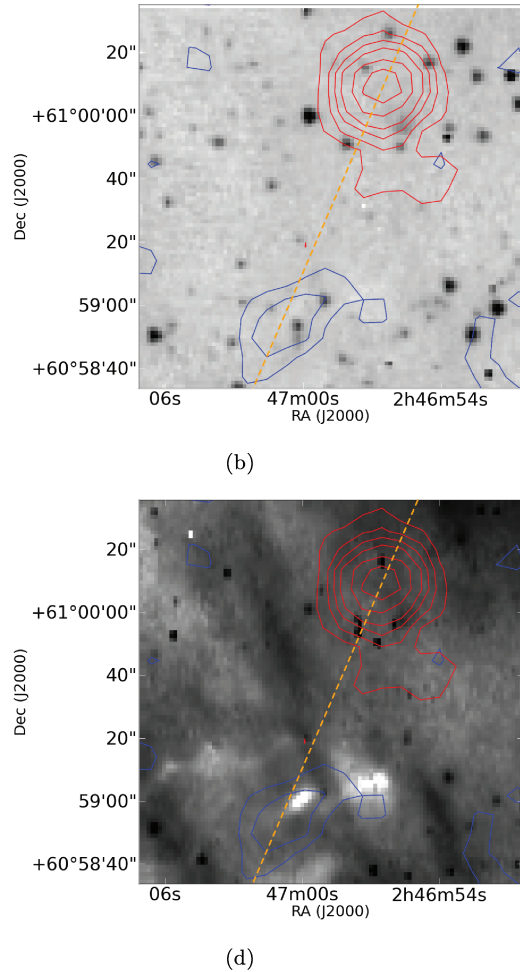
**Figure 5.** Position–velocity diagram, spectra and contour overlays of Outflow 2 (see Fig. 4 for a complete description). While the two lobes are widely separated, there are no nearby lobes that could lead to confusion, so we regard this pair as a reliable bipolar outflow identification.

only have peak velocities  $v \lesssim c_{\text{II}}/4 \approx 2.5 \text{ km s}^{-1}$  in the strong adiabatic shock limit, so that any gas seen with higher-velocity tails are unlikely to be radiation-driven.

Another plausible outflow impostor is the high-velocity tail in a turbulent distribution. However, for a typical molecular cloud, the low temperatures would require very high mach-number shocks ( $\mathcal{M} \gtrsim 10$  assuming  $T_{\text{cloud}} \sim 20 \text{ K}$  and  $v_{\text{flow}} \sim 3 \text{ km s}^{-1}$ ) that in idealized turbulence should be rare and short-lived. It is not known how frequent such high-velocity excursions will be in non-ideal turbulence with gravity (Goodman and Padoan, private communication). Finally, it is less likely for turbulent intermittency to have nearly coincident red and blue lobes, so intermittency can be morphologically excluded in most cases.

### 3.1.1 Comparison to Perseus CO 3–2 observations

We used the HARP CO 3–2 cubes from Hatchell, Fuller & Richer (2007) to evaluate our ability to identify outflows. We selected an outflow that was well-resolved and unconfused, L1448, and evaluated it at both the native sensitivity of the Hatchell et al. (2007) observations and degraded in resolution and sensitivity to match our own. We focus on L1448 IRS2, labelled Outflow 30 in Hatchell et al. (2007). Fig. 7 shows a comparison between the original quality and degraded data.



Integrating over the outflow velocity range, we measure each lobe to be about  $1.6 \times 0.8 \text{ arcmin}^2$  ( $0.14 \times 0.07 \text{ pc}$ ). Assuming a distance to Perseus of 250 pc (e.g. Enoch et al. 2006), we smooth by a factor of 8 by convolving the cube with an FWHM = 111 arcsec Gaussian, then downsample by the same factor of 8 to achieve 6 arcsec square pixels at 2 kpc. The resulting noise was reduced because of the spatial and spectral smoothing and was measured to be  $\approx 0.05 \text{ K}$  in  $0.54 \text{ km s}^{-1}$  channels, which is comparable to the sensitivity in our survey. It is still possible to distinguish the outflows from the cloud in position–velocity space. Each lobe is individually unresolved (long axis  $\sim 12$  arcsec compared to our beam FWHM of 18 arcsec), but the two are separated by  $\gtrsim 20$  arcsec and therefore an overall spatial separation can still be measured. Because they are just barely unresolved at this distance, the lobes’ surface brightnesses are approximately the same at 2 kpc as at 250 pc; if this outflow were seen at a greater distance it would appear fainter.

Hatchell et al. (2007) detected four outflows within this map, plus an additional confused candidate. We note an additional grouping of outflowing material in the north-middle of the map (centred on coordinate  $150 \times 150$  in Fig. 7). In the smoothed version, only three outflows are detected in the blue and two in the red, making flow-counterflow association difficult. The north-central blueshifted component appears to be the counterpart of the red flow when smoothed, although it is clearly the counterpart of the north-west blue flow in the full-resolution image.

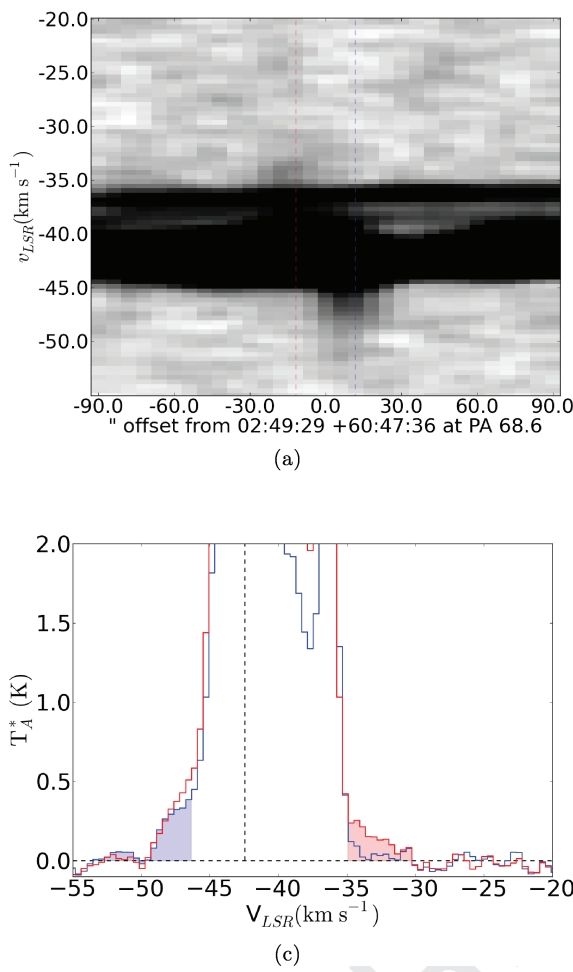
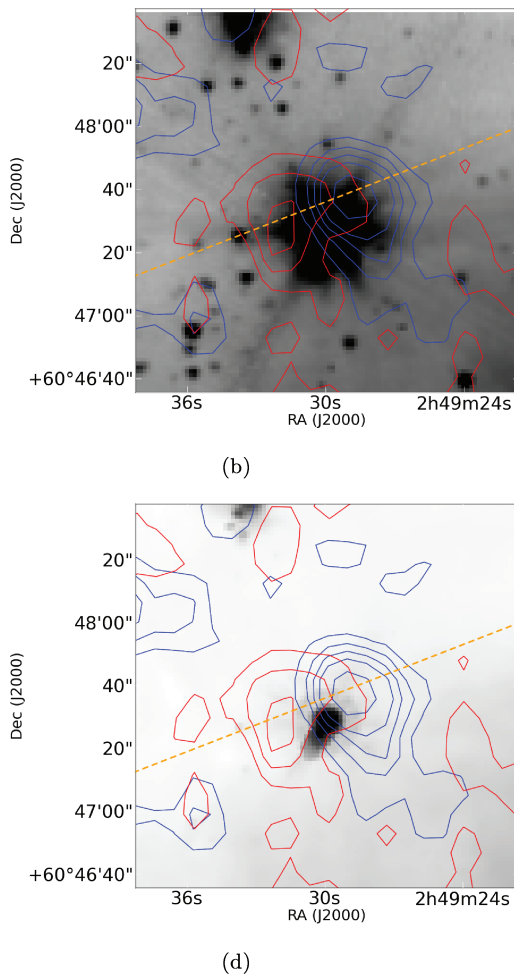


**Figure 6.** Position–velocity diagram, spectra and contour overlays of Outflow 12. Much of the red outflow is lost in the complex velocity profile of the molecular cloud(s), but it is high enough velocity to still be distinguished.

We are therefore able to detect any outflows comparable to L1448 (assuming a favourable geometry), but are likely to see clustered outflows as single or possibly extended lobes and will count fewer lobes than would be detected at higher resolution. Additionally, it is clear from this example that two adjacent outflows with opposite polarity are not necessarily associated, and therefore the outflows’ source(s) may not be between the two lobes.

In order to determine overall detectability of outflows compared to Perseus, we compare to Curtis et al. (2010) in Fig. 8. Out of 29 outflows in their survey with measured ‘lobe lengths’, 22 (71 per cent) were smaller than 128 arcsec which would be below our 18 arcsec resolution if observed at 2 kpc. Even the largest lobes (HRF26R, HRF28R, HRF44B) would only extend  $\sim$ 60 arcsec at 2 kpc. Each lobe in the largest outflow in our survey, Outflow 1, is  $\sim$ 80 arcsec (660 arcsec at 250 pc), but no other individual outflow lobes in W5 are clearly resolved. However, as seen in Fig. 8, many bipolar lobes are *separated* by more than the telescope resolution, and the overall lobe separation distribution (as opposed to the lobe length, which is mostly unmeasured in our sample) in W5 is quite similar to the separation distribution in Perseus. The two-sample KS test gives a 25 per cent probability that they are drawn from the same distribution (the null hypothesis that they are drawn from the same distribution cannot be rejected).

On average, the Curtis et al. (2010) outflow velocities are similar to ours (Fig. 9). We detect lower velocity outflows because we do not



set a strict lower velocity limit criterion. We do not detect the highest velocity outflows most likely because of our poorer sensitivity to the faint high-velocity tips of outflows, although it is also possible that no high-velocity ( $v > 20 \text{ km s}^{-1}$ ) flows exist in the W5 region. Note that the histogram compares quantities that are not directly equivalent: the outflows in Curtis et al. (2010) and our own data are measured out to the point at which the outflow signal is lost, while the ‘region’ velocities are FWHM velocities.

Finally, we use the detectability of outflows in Perseus to inform **our expectations** in W5. Since it appears that we can detect outflows from low-mass protostars with sub-stellar to  $\sim$ 30  $L_\odot$  luminosities at the distance of W5 and these objects should be the most numerous in a standard initial mass function, the distribution of physical properties in W5 outflows should be similar to those in Perseus. However, because W5 is a somewhat more massive cloud ( $M_{\text{W5}} \approx 5 M_{\text{Perseus}}$ <sup>6</sup>), we might expect the high-end of the distribution to extend to higher values of outflow mass, momentum and

Q21

<sup>6</sup>  $M_{\text{W5}}$  is estimated from  $^{13}\text{CO}$ . We also estimate the total molecular mass in W5 using the X-factor and acquire  $M_{\text{W5}} = 5.0 \times 10^4 M_\odot$ , in agreement with Karr & Martin (2003), who estimated a molecular mass of  $4.4 \times 10^4$  from  $^{12}\text{CO}$  using the same X-factor. Koenig et al. (2008) estimated a total gas mass of  $6.5 \times 10^4$  from a Two-Micron All Sky Survey extinction map. The total molecular mass in Perseus is  $M_{\text{Perseus}} \sim 10^4$  (Bally et al. 2008).

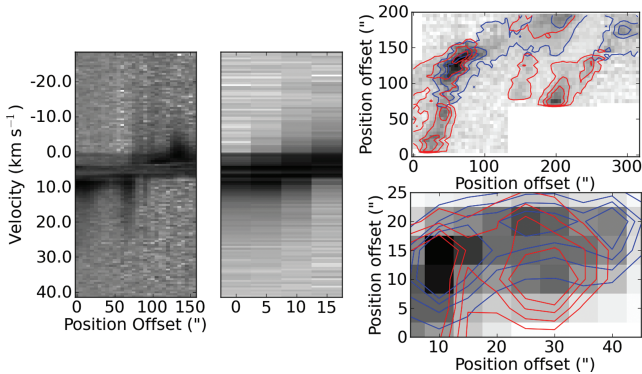


**Figure 7.** Comparison of L1448 seen at a distance of 250 pc (left) versus 2 kpc (middle) with sensitivity 0.5 K and 0.05 K per 0.5  $\text{km s}^{-1}$  channel, respectively. Far left: position–velocity diagram (log scale) of the outflow L1448 IRS2 at its native resolution and velocity. L1448 IRS2 is the rightmost outflow in the contour plots. The position–velocity diagram is rotated 45° from RA/Dec. axes to go along the outflow axis. Middle left: position–velocity diagram (log scale) of the same outflow smoothed and rebinned to be eight times more distant. Top right: the integrated map is displayed at its native resolution (linear scale). The red contours are of the same data integrated from 6.5 to 16  $\text{km s}^{-1}$  and the blue from -6 to 0  $\text{km s}^{-1}$ . Contours are at 1, 3 and 5  $\text{K km s}^{-1}$  ( $\sim 6, 18, 30\sigma$ ). Axes are offsets in arcsec. Because we are only examining the relative detectability of outflows at two distances, we are not concerned with absolute coordinates. Bottom right: the same map as it would be observed at eight times greater distance. Axes are offsets in arcsec assuming the greater distance. Contours are integrated over the same velocity range as above, but are displayed at levels 0.25, 0.50, 0.75, 1.00  $\text{K km s}^{-1}$  ( $\sim 12, 24, 48, 60\sigma$ ). The entire region is detected at high significance, but dominated by confusion. It is still evident that the red and blue lobes are distinct, but they are each unresolved.

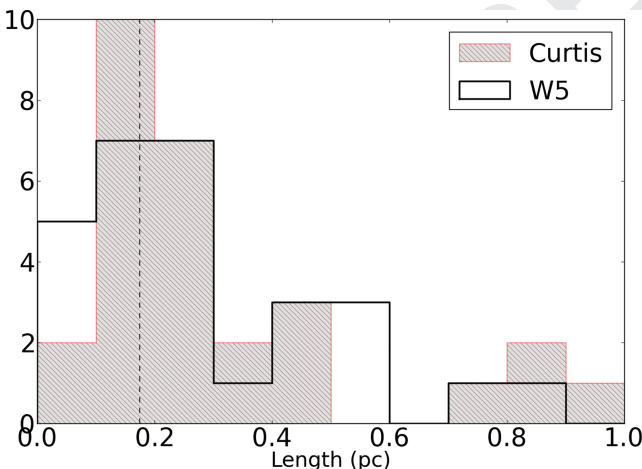


**Figure 8.** Histogram of the measured outflow lobe separations. The grey hatched region shows Curtis et al. (2010) values. The vertical dashed line represents the spatial resolution of our survey. The two distributions are similar.

energy. Since we will likely see clustered outflows confused into a smaller number of distinct lobes, we expect a bias towards higher values of the derived quantities but a lower detection rate.

### 3.1.2 Velocity, column density and mass measurements

Throughout this section, we assume that the CO lines are optically thin and thermally excited. The measured properties are presented in Table 2. These assumptions are likely to be invalid, so we also

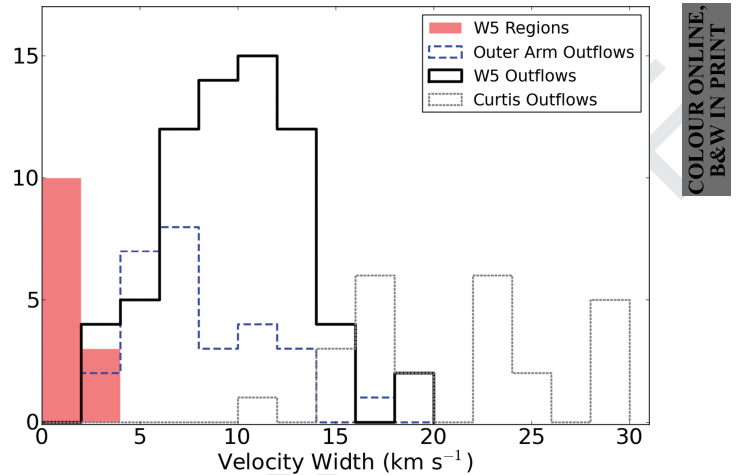


**Figure 9.** Histogram of the outflow linewidths. Black lines: histogram of the measured outflow widths (half-width zero-intensity, measured from the fitted central velocity of the cloud to the highest velocity with non-zero emission). Blue dashed lines: outflow half-width zero-intensity (HWZI) for the outer-arm (non-W5) sample. Solid red shaded: the measured widths (HWHM) of the sub-regions as tabulated in Table 1. Grey dotted: outflow  $v_{\max}$  (HWZI) values for Perseus from Curtis et al. (2010).

discuss the consequences of applying ‘typical’ optical depth corrections to the derived quantities. Because we do not measure optical depths and the optical depth correction for CO 3–2 is less well quantified than for CO 1–0 (Cabrit & Bertout 1990; Curtis et al. 2010),<sup>7</sup> we only present the uncorrected measurements in Table 3.

The outflow velocity ranges were measured by examining both RA–velocity and Dec.–velocity diagrams interactively using the STARLINK GAIA data cube viewing tool. The velocity limits are set to include all outflow emission that is distinguishable from the cloud (i.e. the velocity at which outflow lobes dominate over the Gaussian wing of the cloud emission) down to zero emission. An outflow size (or lobe size, following Curtis et al. 2010) was determined by integrating over the blue and red velocity ranges and creating an elliptical aperture to include both peaks; the position and size therefore have approximately beam-sized ( $\approx 18$  arcsec) accuracy. The integrated outflow maps are shown as red and blue contours in Fig. 5. The velocity centre was computed by fitting a Gaussian to the FCRAO  $^{13}\text{CO}$  spectrum averaged over the elliptical aperture.

The column density is estimated from  $^{12}\text{CO } J = 3–2$  assuming local thermal equilibrium (LTE) and optically thin emission using the equation  $N(\text{H}_2) = 5.3 \times 10^{18} \eta_{\text{mb}}^{-1} \int T_{\text{A}}^*(v) \, dv$  for  $T_{\text{ex}} = 20$  K. The derivation is given in the Appendix. The column density in the lobes is likely to be dominated by low-velocity gas and therefore our dominant uncertainty may be missing low-velocity emission rather than poor assumptions about the optical depth.

The scalar momentum and energy were computed from

$$p = M \frac{\sum T_{\text{A}}^*(v)(v - v_c)\Delta v}{\sum T_{\text{A}}^*(v)\Delta v} \quad (1)$$

$$E = \frac{M}{2} \frac{\sum T_{\text{A}}^*(v)(v - v_c)^2 \Delta v}{\sum T_{\text{A}}^*(v)\Delta v} \quad (2)$$

where  $v_c$  is the  $^{13}\text{CO } 1–0$  centroid velocity. The same assumptions used in determining column density are applied here.

<sup>7</sup> In Curtis et al. (2010), this correction factor ranged from 1.8 to 14.3; Arce et al. (2010) did not enumerate the optical depth correction they used but it is typically around 7 (Cabrit & Bertout 1990).

**Table 1.** Gaussian fit parameters of sub-regions.

Region	Velocity 1 (km s <sup>-1</sup> )	Width 1 (FWHM, km s <sup>-1</sup> )	Amplitude 1 (K)	Velocity 2 (km s <sup>-1</sup> )	Width 2 (FWHM, km s <sup>-1</sup> )	Amplitude 2 (K)
S201	−38.04	3.149	2.35	—	—	—
AFGL 4029	−38.91	3.3605	1.48	—	—	—
LWCas	−38.83	3.478	2.33	—	—	—
W5W	−41.37	3.8775	3.07	−36.16	3.8305	1.90
W5NW	−36.37	3.854	1.6	—	—	—
W5NWpc	−36.37	3.713	1.19	−41.81	4.3475	0.47
W5SW	−42.78	4.136	0.6	−36.34	4.183	0.22
W5S	−40.15	2.914	0.34	−35.76	2.2795	0.40
Inactive1	−42.91	2.6555	0.75	−39.38	4.2065	0.42
Inactive2	−38.94	3.7365	1.2	—	—	—
Empty	−37.81	5.217	0.04	—	—	—
<sup>13</sup> CO fits						
					<sup>13</sup> CO mass (M <sub>⊙</sub> )	<sup>13</sup> CO momentum (M <sub>⊙</sub> km s <sup>-1</sup> )
						<sup>13</sup> CO energy (erg)
S201	−37.97	2.5615	0.56	—	—	8.9 × 10 <sup>46</sup>
AFGL 4029	−38.66	2.35	0.35	—	—	1.4 × 10 <sup>47</sup>
LWCas	−38.75	2.679	0.51	—	—	2.7 × 10 <sup>47</sup>
W5W	−41.23	2.773	1.09	−36.51	3.5485	3.5 × 10 <sup>47</sup>
W5NW	−36.1	3.431	0.7	—	—	6.3 × 10 <sup>47</sup>
W5NWpc	−36.18	3.3135	0.42	−41.44	3.619	1.6 × 10 <sup>48</sup>
W5SW	−42.6	3.807	0.1	−36.15	4.2535	1.1 × 10 <sup>47</sup>
W5S	−39.9	2.444	0.07	−35.48	2.209	1.9 × 10 <sup>46</sup>
Inactive1	−42.58	2.5145	0.1	−38.97	2.82	8.7 × 10 <sup>46</sup>
Inactive2	−38.82	3.196	0.37	—	—	3.2 × 10 <sup>47</sup>
Empty	−38.44	4.7705	0.02	—	—	7.8 × 10 <sup>46</sup>

We estimate an outflow lifetime by taking half the distance between the red and blue outflow centroids divided by the maximum measured velocity difference [ $\Delta v_{\max} = (v_{\max,\text{red}} - v_{\max,\text{blue}})/2$ ],  $\tau_{\text{flow}} = L_{\text{flow}}/(2\Delta v_{\max})$ , where  $L_{\text{flow}}$  refers to the length of the flow. This method assumes that the outflow inclination is 45°; if it is more parallel to the plane of the sky, we overestimate the age, and vice versa. The momentum flux is then  $\dot{P} = p/\tau$ . Similarly, we compute a mass-loss rate by dividing the total outflow mass by the dynamical age, which yields what is likely a lower limit on the mass-loss rate (if the lifetime is underestimated, the mass-loss rate is overestimated, but the outflow mass is always a lower limit because of optical depth and confusion effects).

The dynamical ages are highly suspect since the red and blue lobes are often unresolved or barely resolved, and diffuse emission averaged with the lobe emission can shift the centroid position. Additionally, it is not clear what portion of the outflow corresponds to the centroid: the bow shock or the jet could both potentially dominate the outflow emission. Curtis et al. (2010) discuss the many ways in which the dynamical age can be in error. Our mass-loss rates are similar to those in Perseus *without* correcting our measurements for optical depth, while our outflow masses are an order of magnitude lower. It therefore appears that our dynamical age estimates must be too low, since we have no reason to expect protostars in W5 to be undergoing mass loss at a greater rate than those in Perseus. However, given more reliable dynamical age estimates from higher resolution observations of shock tracers, the mass-loss rates could be corrected and compared to other star-forming regions.

Because the emission was assumed to be optically thin, the mass, column, energy and momentum measurements we present are strictly lower limits. While some authors have computed correction factors to <sup>12</sup>CO 1–0 optical depths (e.g. Cabrit & Bertout 1990), the corrections are different for the 3–2 transition (1.8 to 14.3; Curtis

et al. 2010). Additionally, CO 3–2 may require a correction for sub-thermal excitation because of its higher critical density (the CO 3–2 critical density is 27 times higher than CO 1–0; see Appendix A for modelling of this effect).

Additionally, most of the outflow mass is at the lowest distinguishable velocities in typical outflows (e.g. Arce et al. 2010). It is therefore plausible that in the more turbulent W5 region, a greater fraction of the outflow mass is blended (velocity confused) with the cloud and therefore not included in mass, momentum and energy measurements. This omission could be greater than the underestimate due to poor opacity assumptions.

The total mass of the W5 outflows is  $M_{\text{tot}} \approx 1.5 M_{\odot}$ , substantially lower, even with an optical depth correction of 10 times, than the 163  $M_{\odot}$  reported in Perseus (Arce et al. 2010). Arce et al. (2010) also include a correction factor of 2.5 to account for higher temperatures in outflows and a factor of 2 to account for emission blended with the cloud. The temperature correction is inappropriate for CO 3–2 (see Appendix A, Fig. A1), but the resulting total outflow mass in W5 with an optical depth correction and a factor of 2 confusion correction is about 30  $M_{\odot}$ . In order to make our measurements consistent with a mass of 160  $M_{\odot}$ , a density upper limit in the outflowing gas of  $n(\text{H}_2) < 10^{3.5} \text{ cm}^{-3}$  is required, since a lower gas density results in greater mass for a given intensity (see Appendix A, Fig. A2). However, we expect the total outflow mass in W5 to be greater than in Perseus because of the greater cloud mass, implying that the density in the flows must be even lower, or additional corrections are needed.

The total outflow momentum is  $p_{\text{tot}} \approx 10.9 M_{\odot} \text{ km s}^{-1}$ , versus a quoted 517  $M_{\odot} \text{ km s}^{-1}$  in Perseus (Arce et al. 2010). Arce et al. (2010) included inclination and dissociative shock corrections for the momentum measurements on top of the correction factors already applied to the mass. If these corrections are removed from the

**Table 2.** CO 3–2 outflow measured properties.

Outflow number	Latitude	Longitude	Ellipse major (arcsec)	Ellipse minor (arcsec)	Ellipse PA (°)	Velocity centre (km s <sup>-1</sup> )	Velocity min (km s <sup>-1</sup> )	Velocity max (km s <sup>-1</sup> )	$\int T_A^* dv$ (K km s <sup>-1</sup> )	Bipolar? <sup>a</sup>
1b	136.4437	1.2622	60	27	342	-36.1	-47.6	-40.3	1.0	yc
1r	136.4674	1.2705	49	24	346	-36.1	-31.9	-23.4	1.5	yc
2b	136.4899	1.1904	30	23	299	-35.7	-48.0	-39.7	0.7	yc
2r	136.4743	1.2042	31	28	332	-35.7	-31.7	-23.0	1.3	yc
3	136.475	1.2548	35	25	332	-31.8	-31.8	-26.8	1.3	n
4b	136.5038	1.2623	26	22	35	-36.2	-44.1	-40.1	0.8	yu
4r	136.5109	1.2751	25	22	332	-36.2	-32.4	-28.6	0.9	yu
5r	136.5126	1.2453	24	22	10	-35.3	-31.4	-28.8	0.8	yu
5b	136.5236	1.2524	39	22	3	-35.3	-45.0	-39.2	1.4	yu
6b	136.532	1.228	28	25	332	-35.3	-44.8	-40.0	0.4	yc
6r	136.5327	1.2333	28	20	318	-35.3	-30.6	-24.0	1.0	yc
7b	136.5453	1.2318	24	19	332	-34.9	-47.5	-39.9	1.7	yc
7r	136.5506	1.2383	27	23	314	-34.9	-29.9	-22.7	1.3	yc
8b	136.5799	1.2755	18	14	332	-34.5	-41.5	-39.3	0.6	yc
8r	136.581	1.2601	34	30	332	-34.5	-29.6	-23.9	1.4	yc
9b	136.67	1.2123	30	27	332	-35.0	-44.5	-38.5	1.4	yc
9r	136.6766	1.2059	40	31	332	-35.0	-31.6	-26.7	0.3	yc
10b	136.7172	0.7859	39	24	353	-42.8	-52.6	-47.5	3.3	yc
10r	136.7271	0.7797	31	26	332	-42.8	-38.1	-33.1	4.1	yc
11b	136.8195	1.082	25	24	331	-34.2	-40.7	-37.0	3.1	yc
11r	136.8173	1.0799	24	22	331	-34.2	-31.4	-20.4	1.5	yc
12b	136.8414	1.1512	30	26	332	-40.4	-53.3	-46.2	1.5	yc
12r	136.8479	1.1517	27	25	332	-40.4	-34.6	-30.1	0.9	yc
13	136.8461	0.8426	28	27	332	-31.0	-31.0	-23.5	1.0	n
14	136.8591	1.176	24	23	332	-47.1	-54.5	-47.1	0.8	n
15	136.9443	1.0841	28	18	348	-45.0	-55.0	-45.0	3.1	n
16b	137.3929	0.5977	23	18	333	-40.7	-47.0	-42.6	0.7	yu
16r	137.3981	0.6121	22	19	357	-40.7	-38.7	-35.2	1.9	yu
17b	137.4084	0.6762	20	18	293	-40.3	-57.9	-43.0	2.3	yc
17r	137.412	0.6775	20	18	308	-40.3	-37.6	-30.4	1.1	yc
18b	137.4925	0.6289	16	15	333	-35.5	-39.2	-37.6	1.1	yc
18r	137.4908	0.6292	18	17	307	-35.5	-33.4	-31.0	2.0	yc
19b	137.4815	0.6409	20	17	1	-36.0	-41.9	-38.9	1.3	yc
19r	137.4798	0.6404	20	16	301	-36.0	-33.1	-25.9	0.7	yc
20r	137.5368	1.2792	24	21	332	-37.4	-33.0	-22.5	5.2	yc
20b	137.539	1.279	27	23	17	-37.4	-52.0	-41.8	3.4	yc
21b	137.6152	1.3543	31	28	322	-39.5	-52.0	-43.7	4.5	yc
21r	137.6169	1.3585	31	18	4	-39.5	-35.2	-30.0	1.2	yc
22	137.6213	1.506	27	21	293	-40.3	-46.0	-40.3	2.1	n
23b	137.6389	1.5251	21	14	331	-38.5	-42.5	-40.5	1.6	yc
23r	137.6449	1.5194	19	12	331	-38.5	-36.5	-32.0	1.9	yc
24r	137.7094	1.4824	20	20	331	-38.2	-33.8	-25.4	4.2	yc
24b	137.7146	1.4809	25	19	292	-38.2	-50.0	-42.7	4.4	yc
25b	138.1398	1.6858	39	26	282	-38.8	-49.5	-43.2	0.6	yc
25r	138.142	1.6884	43	35	11	-38.8	-34.3	-27.5	1.7	yc
26b	138.2913	1.5538	29	29	355	-38.7	-52.0	-47.4	1.2	yc
26r	138.2966	1.5564	28	28	330	-38.7	-30.0	-20.0	4.2	yc
27	138.3017	1.5689	26	25	330	-30.0	-30.0	-22.0	1.8	n
28	138.3042	1.5437	20	19	330	-43.3	-46.1	-43.3	1.4	n
29	138.3053	1.5537	22	20	330	-45.3	-51.6	-45.3	2.5	n
30	138.3115	1.5443	26	26	330	-33.0	-33.0	-29.2	1.2	n
31	138.3184	1.5566	26	25	330	-44.4	-49.1	-44.4	1.1	n
32	138.3213	1.5658	27	27	330	-31.7	-31.7	-27.0	1.4	n
33b	138.3618	1.5073	28	26	330	-39.4	-49.5	-44.0	1.3	yc
33r	138.3642	1.4959	29	21	330	-39.4	-34.7	-25.8	2.0	yc
34r	138.4779	1.6137	22	21	330	-36.9	-33.1	-29.1	0.5	yc
34b	138.4768	1.6142	21	20	330	-36.9	-43.6	-40.6	0.8	yc
35r	138.4998	1.6496	22	20	4	-37.5	-31.3	-24.1	1.4	yc
35b	138.5021	1.6458	23	21	330	-37.5	-49.5	-43.6	1.3	yc
36b	138.5034	1.6654	35	26	5	-37.5	-50.4	-42.3	1.2	yc
36r	138.5061	1.6576	22	21	330	-37.5	-32.6	-26.7	1.4	yc

**Table 2 – continued**

Outflow number	Latitude	Longitude	Ellipse major (arcsec)	Ellipse minor (arcsec)	Ellipse PA (°)	Velocity centre (km s <sup>-1</sup> )	Velocity min (km s <sup>-1</sup> )	Velocity max (km s <sup>-1</sup> )	$\int T_A^* dv$ (K km s <sup>-1</sup> )	Bipolar? <sup>a</sup>
37r	138.5208	1.6618	27	22	330	-38.5	-33.5	-31.4	0.6	yc
37b	138.5241	1.6667	23	23	18	-38.5	-47.0	-43.6	0.6	yc
38b	137.4983	0.6062	16	15	333	-36.1	-39.2	-38.5	0.8	yc
38r	137.4977	0.6055	15	14	307	-36.1	-33.7	-32.5	0.5	yc
39b	138.1506	0.7724	23	16	321	-38.8	-45.3	-41.0	2.0	yc
39r	138.1591	0.7713	17	13	304	-38.8	-36.6	-34.7	0.7	yc
40	138.1356	0.7634	22	18	4	-36.0	-36.0	-27.6	2.2	n

Measured properties of the outflows.

<sup>a</sup> Is the outflow part of a bipolar pair? yc = yes, confident; yu = yes, uncertain; n = no.

Perseus momentum total (except for optical depth, which is variable in their data and therefore cannot be removed), the uncorrected outflow momentum in Perseus would be about  $74 M_\odot \text{ km s}^{-1}$ . The W5 outflow momentum, if corrected with a ‘typical’ optical depth in the range 7–14, would match or exceed this value. If an additional CO 3–2 excitation correction (in the range 1–20) is applied, the W5 outflow momentum would significantly exceed that in Perseus.

Assuming a turbulent linewidth  $\Delta v \sim 3 \text{ km s}^{-1}$  (approximately the smallest FWHM linewidth observed), the total turbulent momentum in the ambient cloud is  $p = M_{\text{tot}} \Delta v = 1.3 \times 10^5 M_\odot \text{ km s}^{-1}$ , which is  $\sim 10^5$  times the measured outflow momentum – the outflows detected in our survey cannot be the sole source of the observed turbulent linewidths, even if corrected for optical depth and missing mass.

Table 1 presents the turbulent momentum for each sub-region computed by multiplying the measured velocity width by the integrated  $^{13}\text{CO}$  mass. Even if the outflow measurements are orders of magnitude low because of optical depth, cloud blending, sub-thermal excitation and other missing-mass considerations, outflows contribute negligibly to the total momentum of high-velocity gas in W5. This result is unsurprising, as there are many other likely sources of energy in the region such as stellar wind bubbles and shock fronts between the ionized and molecular gas. Additionally, in regions unaffected by feedback from the H II region (e.g. W5NW), cloud–cloud collisions are a possible source of energy.

Fig. 10 displays the distribution of measured properties and compares them to those derived in the COMPLETE (Arce et al. 2010) and Curtis et al. (2010) HARP CO 3–2 surveys of Perseus. Our derived masses are substantially lower than those in Arce et al. (2010) even if corrected for optical depth, but our momenta are similar to the COMPLETE Perseus Outflow Candidate (CPOC) sample and our energies are higher, indicating a bias towards detecting mass at high velocities. The bias is more heavily towards high velocities than the CO 1–0 used in Arce et al. (2010). The discrepancy between our values and those of Arce et al. (2010) and Curtis et al. (2010) can be partly accounted for by the optical depth correction applied in those works:  $^{13}\text{CO}$  was used to correct for opacity at low velocities, where most of the outflow mass is expected. Those works may also have been less affected by blending because of the smaller cloud linewidths in Perseus.

The momentum flux and mass-loss rate are compared to the values derived in Perseus by Hatchell et al. (2007) and Curtis et al. (2010) in Figs 11 and 12. Both of our values are computed using the dynamical time-scale  $\tau_d$  measured from outflow lobe separation, while the Hatchell et al. (2007) values are derived using a more direct momentum-flux measurement in which the momentum-flux contribution of each pixel in the resolved outflow map is

considered. The derived momentum fluxes (Fig. 11) are approximately consistent with the Curtis et al. (2010) Perseus momentum fluxes; Curtis et al. (2010) measure momentum fluxes in a range  $1 \times 10^{-6} < \dot{P} < 7 \times 10^{-4} M_\odot \text{ km s}^{-1} \text{ yr}^{-1}$ , higher than our measured  $6 \times 10^{-7} < \dot{P} < 1 \times 10^{-4} M_\odot \text{ km s}^{-1} \text{ yr}^{-1}$  by approximately the opacity correction they applied. As seen in Fig. 11, the Hatchell et al. (2007) momentum-flux measurements in Perseus cover a much lower range  $6 \times 10^{-8} < \dot{P} < 2 \times 10^{-5} M_\odot \text{ km s}^{-1} \text{ yr}^{-1}$  and are not consistent with our measurements. This disagreement is most likely because of the difference in method. The W5 outflows exhibit substantially higher mass-loss rates and momentum fluxes if we assume a factor of 10 opacity correction, as expected from our bias towards higher-velocity, higher-mass flows.

### 3.2 Structure of the W5 molecular clouds: a thin sheet?

The W5 complex extends  $\sim 1.6 \times 0.7$  within  $20^\circ$  of parallel with the galactic plane. At the assumed distance of 2 kpc, it has a projected length of  $\sim 60$  pc (Fig. 2). In the 8  $\mu\text{m}$  band (Fig. 1), the region appears to consist of two blown-out bubbles with  $\sim 10$ – $15$  pc radii centred on  $\ell = 138.1, b = 1.4$  and  $\ell = 137.5, b = 0.9$ . While the bubbles are filled in with low-level far-infrared emission, there is no CO detected down to a  $3\sigma$  limit of  $3.0 \text{ K km s}^{-1}$  ( $^{12}\text{CO}$  1–0),  $2.4 \text{ K km s}^{-1}$  ( $^{12}\text{CO}$  3–2, excepting a few isolated clumps) and  $1.5 \text{ K km s}^{-1}$  ( $^{13}\text{CO}$  1–0). Using the X-factor (the CO-to-H<sub>2</sub> conversion factor) for  $^{12}\text{CO}$   $N(\text{H}_2) = 3.6 \times 10^{20} \text{ cm}^{-2}/(\text{K km s}^{-1})$ , we derive an upper limit  $N(\text{H}_2) < 1.1 \times 10^{21} \text{ cm}^{-2}$ , or  $A_V \lesssim 0.6$ . Individual ‘wisps’ and ‘clumps’ of CO can sometimes be seen, particularly towards the cloud edges, but in general the bubbles are absent of CO gas.

Given such low column limits, the W5 cloud must be much smaller along the line of sight than its  $\sim 50$  pc size projected on the sky. Alternately, along the line of sight, the columns of molecular gas are too low for CO to self-shield, and it is therefore destroyed by the UV radiation of W5’s O-stars. In either case, there is a significant excess of molecular gas in the plane of the sky compared to the line of sight, which makes W5 an excellent location to perform unobscured observations of the star formation process. The implied thin geometry of the W5 molecular cloud may therefore be similar to the bubbles observed by Beaumont & Williams (2010), but on a larger scale.

There is also morphological evidence supporting the face-on hypothesis. In the AFGL 4029 region (Section 4.2) and all along the south of W5, there are ridges with many individual cometary ‘heads’ pointing towards the O-stars that are unconfused along the line of sight. This sort of separation would not be expected if we were looking through the clouds towards the O-stars. W5W, however,

**Table 3.** CO 3–2 outflow derived properties.

Outflow number	Mass ( $M_{\odot}$ )	Momentum ( $M_{\odot} \text{ km s}^{-1}$ )	Energy ( $10^{42} \text{ erg}$ )	Dynamical age ( $10^4 \text{ yr}$ )	Momentum flux ( $10^{-6} M_{\odot} \text{ km s}^{-1} \text{ yr}^{-1}$ )
1b	0.034	0.26	21.1	7.0	7.2
1r	0.04	0.24	17.3	7.0	7.2
2b	0.011	0.07	4.9	5.4	4.4
2r	0.025	0.17	13.0	5.4	4.4
3	0.025	0.12	5.8	—	—
4b	0.01	0.06	4.0	7.2	1.5
4r	0.011	0.04	1.8	7.2	1.5
5r	0.01	0.04	2.0	4.5	4.0
5b	0.025	0.14	8.0	4.5	4.0
6b	0.007	0.04	3.0	1.7	8.1
6r	0.013	0.09	6.8	1.7	8.1
7b	0.017	0.13	10.5	2.4	10.9
7r	0.018	0.13	9.7	2.4	10.9
8b	0.003	0.02	0.9	4.9	4.5
8r	0.032	0.2	13.2	4.9	4.5
9b	0.025	0.13	7.2	3.9	4.2
9r	0.009	0.04	1.8	3.9	4.2
10b	0.068	0.41	25.7	3.9	22.0
10r	0.074	0.45	28.0	3.9	22.0
11b	0.042	0.17	7.2	0.7	35.3
11r	0.017	0.09	5.9	0.7	35.3
12b	0.026	0.14	8.7	1.8	15.2
12r	0.014	0.13	12.7	1.8	15.2
13	0.016	0.1	5.8	—	—
14	0.01	0.06	4.1	—	—
15	0.036	0.24	17.3	—	—
16b	0.006	0.03	1.2	11.1	0.7
16r	0.018	0.05	1.3	11.1	0.7
17b	0.019	0.12	9.4	1.4	10.6
17r	0.009	0.03	0.7	1.4	10.6
18b	0.006	0.02	0.5	1.4	4.0
18r	0.013	0.04	1.0	1.4	4.0
19b	0.011	0.05	2.4	0.7	9.6
19r	0.005	0.01	0.2	0.7	9.6
20r	0.059	0.5	46.3	0.5	156.0
20b	0.047	0.33	26.6	0.5	156.0
21b	0.086	0.58	41.4	1.7	39.1
21r	0.014	0.08	4.3	1.7	39.1
22	0.027	0.1	4.3	—	—
23b	0.011	0.03	0.9	4.5	1.3
23r	0.01	0.03	1.0	4.5	1.3
24r	0.037	0.3	26.1	1.7	34.1
24b	0.047	0.28	18.3	1.7	34.1
25b	0.014	0.09	6.8	1.0	42.8
25r	0.056	0.35	23.0	1.0	42.8
26b	0.023	0.24	26.1	1.1	98.3
26r	0.072	0.85	106.0	1.1	98.3
27	0.026	0.09	4.5	—	—
28	0.012	0.07	4.6	—	—
29	0.024	0.06	2.1	—	—
30	0.018	0.12	8.0	—	—
31	0.016	0.03	0.7	—	—
32	0.023	0.18	14.5	—	—
33b	0.022	0.14	10.1	3.0	11.4
33r	0.026	0.2	16.1	3.0	11.4
34r	0.005	0.03	1.7	0.7	8.4
34b	0.007	0.03	1.2	0.7	8.4
35r	0.013	0.12	11.6	1.3	18.7
35b	0.014	0.12	11.0	1.3	18.7
36b	0.025	0.19	15.8	2.7	10.7
36r	0.014	0.1	6.8	2.7	10.7

**Table 3 – continued**

Outflow number	Mass ( $M_{\odot}$ )	Momentum ( $M_{\odot} \text{ km s}^{-1}$ )	Energy ( $10^{42} \text{ erg}$ )	Dynamical age ( $10^4 \text{ yr}$ )	Momentum flux ( $10^{-6} M_{\odot} \text{ km s}^{-1} \text{ yr}^{-1}$ )
37r	0.008	0.04	1.6	2.1	4.3
37b	0.007	0.06	4.2	2.1	4.3
38b	0.005	0.01	0.4	0.9	2.3
38r	0.002	0.01	0.1	0.9	2.3
39b	0.017	0.07	2.8	7.5	1.0
39r	0.004	0.01	0.3	7.5	1.0
40	0.019	0.08	3.5	—	—

Derived properties of the outflows in the optically **thin limit**.Typical optical depth corrections for  $^{12}\text{CO}$  3–2 are in the range 7–14 (Curtis et al. 2010).The correction for velocity confusion is  $\gtrsim 2$  but poorly constrained (Arce et al. 2010).

Finally, an excitation correction in the range 1–20 is likely required as described in the Appendix.

The mass and momentum values can be multiplied by these factors to acquire the corrected values.

The energy is weighted more heavily towards high-velocity, low-optical-depth gas, so the correction factor is likely to be lower.

presents a counterexample in which there are two clouds along the line of sight that may well be masking a more complex geometry.

Q24

## 4 SUB-REGIONS

Individual regions were selected from the mosaic for comparison. All regions with multiple outflows and indicators of star formation activity were named and included as regions for analysis. Additionally, three ‘inactive’ regions were selected based on the presence of  $^{13}\text{CO}$  emission but the lack of outflows in the  $^{12}\text{CO}$  3–2 data. Finally, two regions devoid of CO emission were selected as a baseline comparison and to place upper limits on the molecular gas content of the east and west ‘bubbles’. The regions are identified on the integrated  $^{13}\text{CO}$  image in Fig. 3.

Average spectra were taken of each ‘region’ within the indicated box. Gaussians were fit to the spectrum to determine linewidths and centres (Fig. 13, Table 1). Gaussian fits were necessary because in many locations there are at least two velocity components, so the second moment (the ‘intensity-weighted dispersion’) is a poor estimator of linewidth. Widths ranged from  $v_{\text{FWHM}} = 2.3$  to  $6.2 \text{ km s}^{-1}$  (Fig. 9).

### 4.1 Sh 2-201

Sh 2-201 is an H II region and is part of the same molecular cloud as the bright-rimmed clouds in W5E, but it does not share a cometary shape with these clouds (Fig. 14). Instead, it is internally heated and has its own ionizing source (Felli, Hjellming & Cesaroni 1987). The AFGL 4029 cloud edge is at a projected distance of  $\sim 7 \text{ pc}$  from the nearest exposed O-star, and the closest illuminated point in the *Spitzer* 8 and 24  $\mu\text{m}$  maps is at a projected distance of  $\sim 5 \text{ pc}$ . The star-forming process must therefore have begun before radiation-driven shocks from the W5 O-stars could have impacted the cloud.

### 4.2 AFGL 4029

AFGL 4029 is a young cluster embedded in a cometary cloud (Fig. 15). There is one clear bipolar outflow and six single-lobed

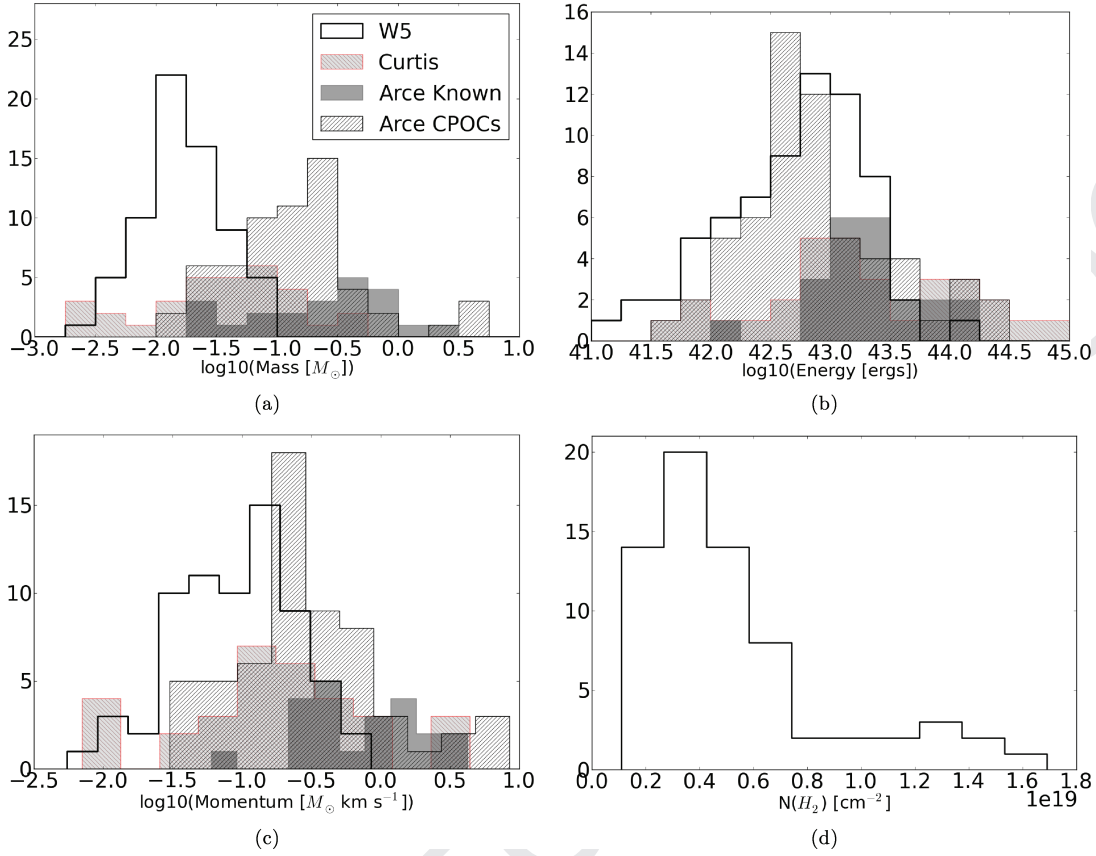


**Figure 10.** Histograms of outflow physical properties. The solid unfilled lines are the W5 outflows (this paper), the forward-slash hashed lines show Arce et al. (2010) CPOCs; the dark grey shaded region shows Arce et al. (2010) values for known outflows in Perseus and the light grey, backslash-hashed regions show Curtis et al. (2010) CO 3–2 outflow properties. The outflow masses measured in Perseus are systematically higher partly because both surveys corrected for line optical depth using  $^{13}\text{CO}$ . The medians of the distributions are 0.017, 0.044, 0.33 and 0.14  $M_\odot$  for W5, Curtis, Arce Known and Arce CPOCs, respectively, which implies that an optical depth and excitation correction factor of 2.5–20 would be required to make the distributions agree (although W5, being a more massive region, might be expected to have more massive and powerful outflows). It is likely that CO 3–2 is sub-thermally excited in outflows, and CO outflows may be destroyed by UV radiation in the W5 complex while they easily survive in the lower-mass Perseus region, which are other factors that could push the W5 mass distribution lower.

flows that cannot be unambiguously associated with an opposite direction counterpart. The cluster is mostly unresolved in the data presented here and is clearly the most active CO clump in W5. It contains a cluster of at least 30 B-stars (Deharveng et al. 1997). The outflows from this region have a full width  $\Delta v \approx 30 \text{ km s}^{-1}$ , which is entirely inconsistent with a radiation-driven inflow or outflow since it is greater than the sound speed in the ionized medium.

The northeast cometary cloud is strongly affected by the W5 H $\alpha$  region. It has an outflow in the head of the cloud (Fig. 16), and the cloud shows a velocity gradient with distance from the H $\alpha$  region. The polarity of the gradient suggests that the cometary cloud must be on the far side of the ionizing O-star along the line of sight assuming that the H $\alpha$  region pressure is responsible for accelerating the cloud edge.

### 4.3 W5 ridge

The W5 complex consists of two H $\alpha$  region bubbles separated by a ridge of molecular gas (Fig. 17). This ridge contains the LW Cas optical nebula, a reflection nebula around the variable star LW Cas, on its east side and an X-shaped nebula on the west. The east portion of LW Cas Nebula is bright in both the continuum and CO  $J = 3–2$  but lacks outflows (see Fig. 17). The east portion also has the highest average peak antenna temperature, suggesting

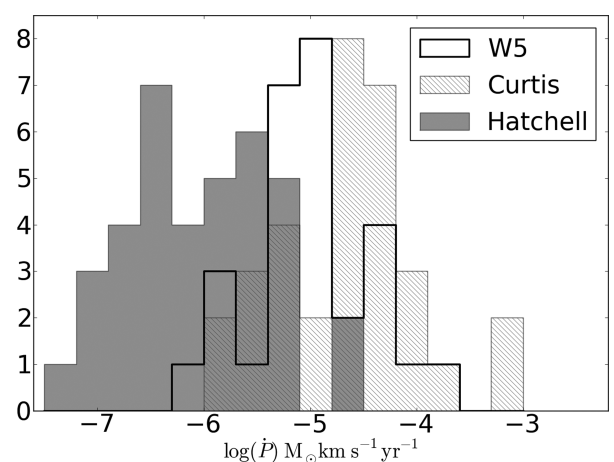


**Figure 11.** Histogram of the measured outflow momentum fluxes. The black thick line shows our data; the grey shaded region shows the Hatchell et al. (2007) data and the hatched region shows Curtis et al. (2010) values. Our measurements peak squarely between the two Perseus JCMT CO 3–2 data sets, although the Curtis et al. (2010) result include an opacity correction that our data do not, suggesting that our results are likely consistent with Curtis et al. (2010) but inconsistent with the Hatchell et al. (2007) direct measurement method.

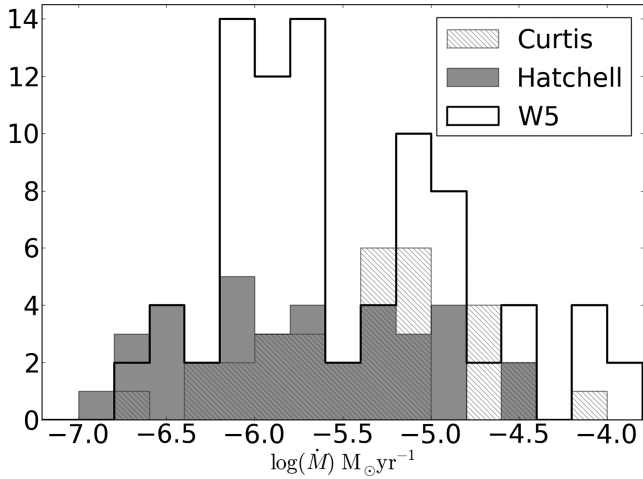


**Figure 12.** Histogram of the measured mass loss rate. The black thick line shows our data, while the grey shaded region shows the Hatchell et al. (2007) data, which are simply computed by  $\dot{M} = \dot{P} \times 10/5 \text{ km s}^{-1}$ , where the factor of 10 is a correction for opacity. Our mass-loss rates are very comparable to those of Hatchell et al. (2007), but different methods were used so the comparison may not be physically meaningful. Curtis et al. (2010) (hatched) used a dynamical time method similar to our own and also derived similar mass-loss rates, although their mass measurements have been opacity-corrected using the  $^{13}\text{CO}$  3–2 line. Because our mass-loss rates agree reasonably with Perseus, but our outflow mass measurements are an order of magnitude low, we believe our dynamical age estimates to be too small.

that the gas temperature in this region is substantially higher than in the majority of the W5 complex (higher spatial densities could also increase the observed  $T_A$ , but the presence of nearby heating sources makes a higher temperature more plausible). It is possible that high gas temperatures are suppressing star formation in the cloud. Alternately, the radiation that is heating the gas may destroy any outflowing CO, which is more likely assuming the two Class I objects identified in this region by Koenig et al. (2008) are genuine protostars.

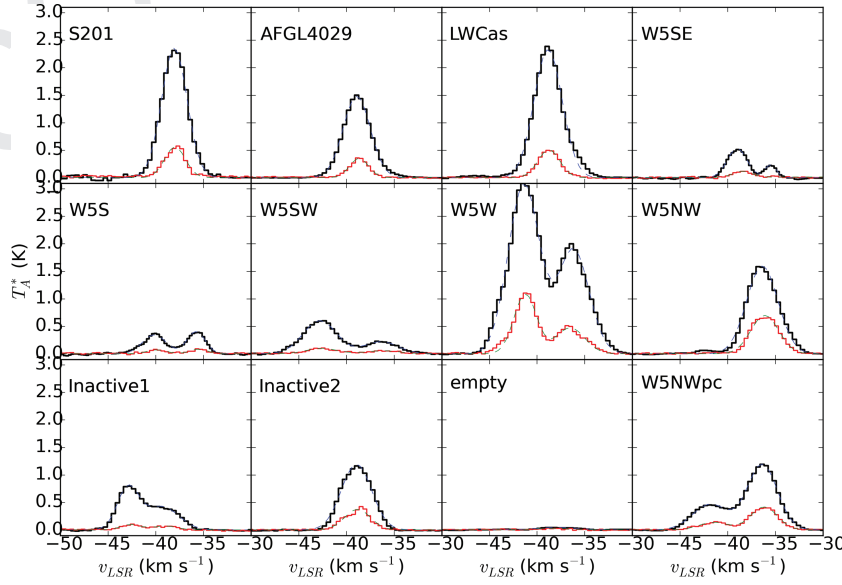


**Figure 13.** Spatially averaged spectra of the individual regions analysed.  $^{12}\text{CO}$  3–2 is shown by thick black lines and  $^{13}\text{CO}$  1–0 is shown by thin red lines. Gaussian fits are overplotted in blue and green dashed lines, respectively. The fit properties are given in Table 1.

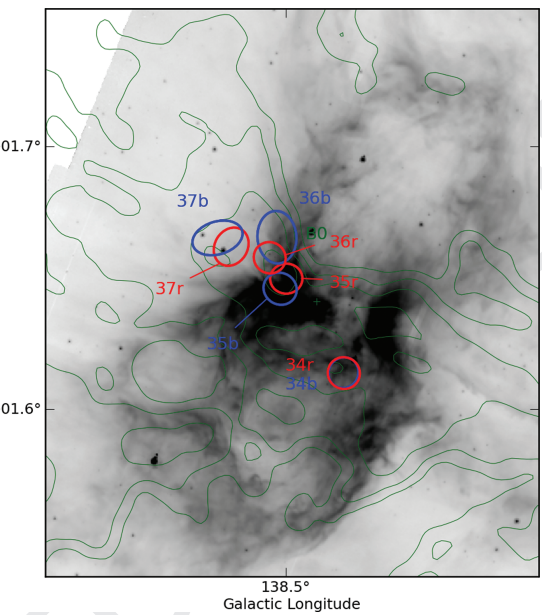


**Figure 14.** Small-scale map of the Sh 2-201 region plotted with CO 3–2 contours integrated from  $-60$  to  $-20 \text{ km s}^{-1}$  at levels 3, 7.2, 17.3, 41.6 and  $100 \text{ K km s}^{-1}$ . The IRAC 8  $\mu\text{m}$  image is displayed in inverted log scale from 800 to  $8000 \text{ MJy sr}^{-1}$ . Contours of the CO 3–2 cube integrated from  $-60$  to  $-20 \text{ km s}^{-1}$  are overlaid at logarithmically spaced levels from 3 to  $100 \text{ K km s}^{-1}$  (3.0, 7.2, 17.3, 41.6, 100;  $\sigma \approx 0.7 \text{ K km s}^{-1}$ ). The ellipses represent the individual outflow lobe apertures mentioned in Section 3.1.2.

The ridge is surprisingly faint in H I 21 cm emission compared to the two H II regions (Fig. 18) considering its 24  $\mu\text{m}$  surface brightness. The integrated H I intensity from  $-45$  to  $-35 \text{ km s}^{-1}$  is  $\sim 800 \text{ K km s}^{-1}$ , whereas in the H II region bubble it is around  $1000 \text{ K km s}^{-1}$ . The CO-bright regions show lower levels of emission similar to the ridge at  $700$ – $800 \text{ K km s}^{-1}$ . However, the ridge contains no CO gas and very few young stars (fig. 7 in Koenig et al. 2008). It is possible that the ridge contains cool H I but has very low column densities along the direction pointing towards the O-stars, in which

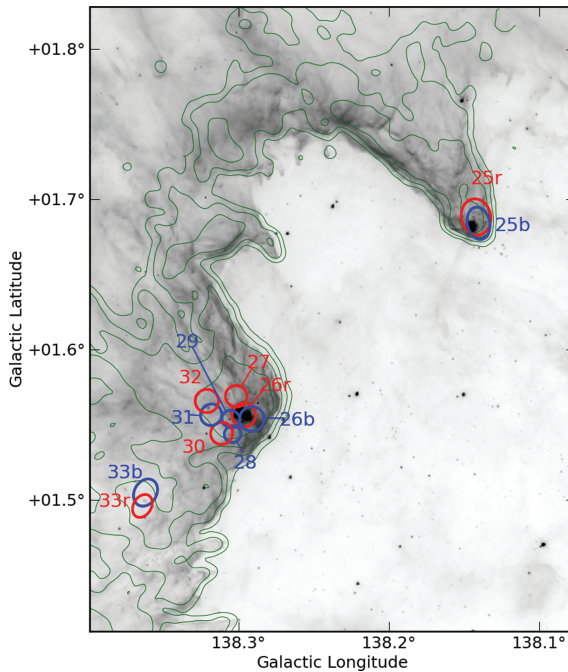


**Figure 15.** Small-scale map of the AFGL 4029 region plotted with CO 3–2 contours integrated from  $-60$  to  $-20 \text{ km s}^{-1}$  at levels 3, 7.2, 17.3, 41.6 and  $100 \text{ K km s}^{-1}$ . The IRAC 8  $\mu\text{m}$  image is displayed in inverted log scale from 800 to 8000  $\text{MJy sr}^{-1}$ . Contours of the CO 3–2 cube integrated from  $-60$  to  $-20 \text{ km s}^{-1}$  are overlaid at logarithmically spaced levels from 3 to  $100 \text{ K km s}^{-1}$  (3, 7.2, 17.3, 41.6, 100;  $\sigma \approx 0.7 \text{ K km s}^{-1}$ ). Outflows 26–32 are ejected from a forming dense cluster. A diagram displaying the kinematics of the northern cometary cloud is shown in Fig. 16.

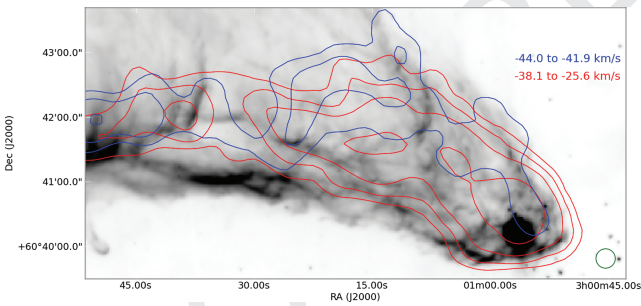


**Figure 16.** The northeast cometary cloud. Contours are shown at 0.5, 1, 2 and  $5 \text{ km s}^{-1}$  integrated over the ranges  $-44.0$  to  $-41.9 \text{ km s}^{-1}$  (blue) and  $-38.1$  to  $-35.6 \text{ km s}^{-1}$  (red). There is a velocity gradient across the tail, suggesting that the front edge is being pushed away along the line of sight.

case the self-shielding is too little to prevent CO dissociation. This ridge may therefore be an excellent location to explore the transition from molecular to atomic gas under the influence of ionizing radiation in conditions different from high-density photodissociation (photon-dominated) regions.

We examine Outflow 20 as a possible case for pressure-driven implosion (radiation, RDI, or gas pressure, PDI) by examining the relative time-scales of the outflow driving source and the H II-region-driven compression front. A typical molecular outflow source (Class 0 or I) has a lifetime of  $\sim 5 \times 10^5 \text{ yr}$  (Evans et al. 2009). Given that there is an active outflow at the head of this cloud, we use 0.5 Myr as an upper limit. The approximate distance from this source to the cloud front behind it is  $\sim 3.3 \text{ pc}$ . If we assume the

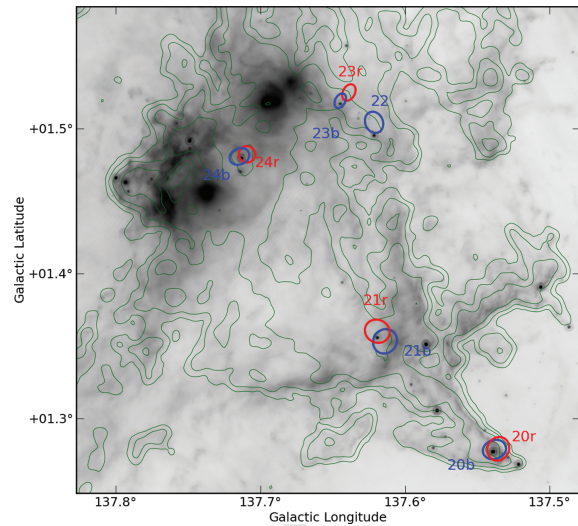


**Figure 17.** Small-scale map of the LW Cas nebula plotted with CO 3–2 contours integrated from  $-60$  to  $-20 \text{ km s}^{-1}$  at levels 3, 7.2, 17.3, 41.6 and  $100 \text{ K km s}^{-1}$ . The feature containing outflows 20 and 21 is the X-shaped ridge referenced in Section 4.3. This sub-region is notable for having very few outflows associated with the most significant patches of CO emission. The gas around it is heated on the left side by the O7V star HD 18326 ( $D_{\text{proj}} = 8.5 \text{ pc}$ ), suggesting that this gas could be substantially warmer than the other molecular clouds in W5.

cloud front has been pushed at a constant speed  $v \leq c_{\text{II}} \approx 10 \text{ km s}^{-1}$ , we derive a lower limit on its age of 0.3 Myr. While these limits allow for the protostar to be older than the compression front by up to 0.2 Myr, it is likely that the compression front moved more slowly (e.g.  $3 \text{ km s}^{-1}$  if it was pushed by a D-type shock front) and that the protostar is not yet at the end of its lifetime – it is very plausible that this source was born in a radiation-driven implosion.

#### 4.4 Southern pillars

There are three cometary clouds that resemble the ‘elephant trunk’ nebula in IC 1396 (Fig. 19). Each of these pillars contains evidence of at least one outflow in the head of the cloud (see the supplementary materials, outflows 16–19 and 38). These pillars are low-mass and isolated; there is no other outflow activity in southern W5. However, because of the bright illumination on their northern edges and robust star formation tracers, these objects present a reasonable case for triggered star formation by the RDI mechanism.

The kinematics of these cometary clouds suggest that they have been pushed in different directions by the H II region (Fig. 19). The central cometary cloud (Fig. 19b) has two tails. The southwest tail emission peaks around  $-39.5 \text{ km s}^{-1}$  and the southeast tail peaks at  $-41.5 \text{ km s}^{-1}$ , while the head is peaked at an intermediate  $-40.5 \text{ km s}^{-1}$ . These velocity shifts suggest that the gas is being accelerated perpendicular to the head–tail axis and that the southeast tail is on the back side of the cometary head, while the southwest tail is on the front side. The expanding H II region is crushing this head–tail system.

The southeast cometary cloud (Fig. 19a) peaks at  $-35.0 \text{ km s}^{-1}$ . There are no clearly separated CO tails as in the central cloud, but there is a velocity shift across the tail, in which the west (right) side is blueshifted compared to the east (left) side, which is the opposite sense from the central cometary cloud.

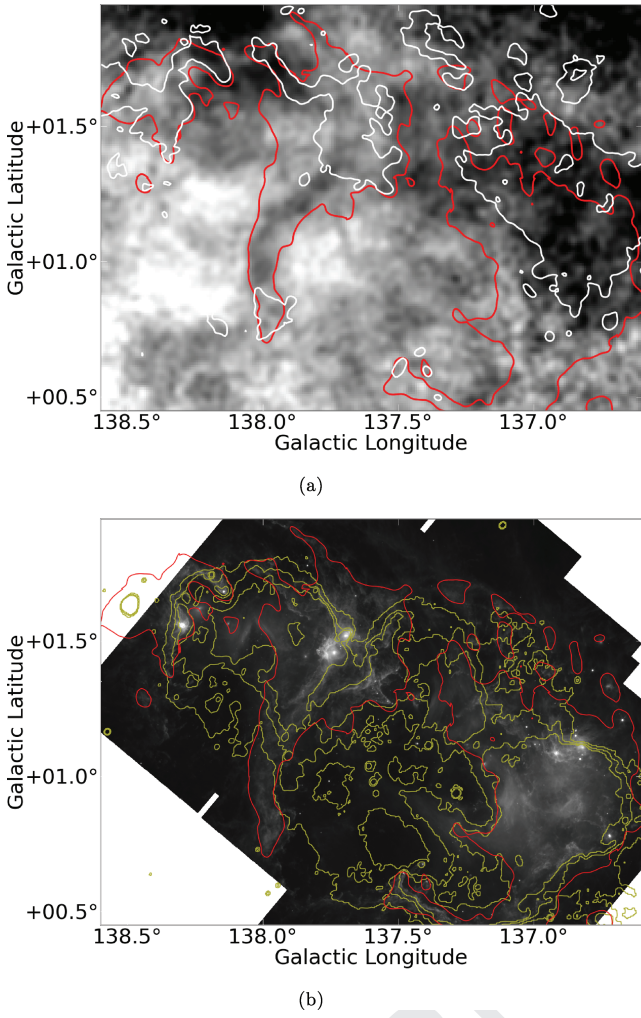


**Figure 18.** Top: the DRAO 21 cm H<sub>1</sub> map integrated from  $-45$  to  $-35$  km s $^{-1}$  displayed in grey-scale from 700 (black) to 1050 (white) K km s $^{-1}$  with IRAS 100  $\mu$ m contours (red, 40 MJy sr $^{-1}$ ) and  $^{12}\text{CO}$  1–0 contours integrated over the same range (white, 4 K km s $^{-1}$ ) overlaid. The ridge of IRAS 100  $\mu$ m emission at  $\ell = 138.0$  coincides with a relative lack of H<sub>1</sub> emission at these velocities, suggesting either that there is less or colder gas along the ridge. Bottom: the *Spitzer* 24  $\mu$ m map with 21 cm continuum contours at 6, 8 and 10 MJy sr $^{-1}$  overlaid. The IRAS contours are also overlaid to provide a reference for comparing the two figures and to demonstrate that the H<sub>II</sub> region abuts the cold H<sub>1</sub> area. The moderate excess of continuum emission implies a somewhat higher electron density along the line of sight through the ridge.

The southwest cometary cloud (Fig. 19c) peaks at  $-40.3$  km s $^{-1}$  and has weakly defined tails similar to the central cloud. Both of its tails are at approximately the same velocity ( $-42.5$  km s $^{-1}$ ).

The kinematics of these tails provide some hints of their 3D structure and location in the cloud. Future study to compare the many cometary flows in W5 to physical models and simulations is warranted. Since these flows are likely at different locations along the line of sight (as required for their different velocities), an analysis of their ionized edges may allow for more precise determination of the full 3D structure of the clouds relative to their ionizing sources.

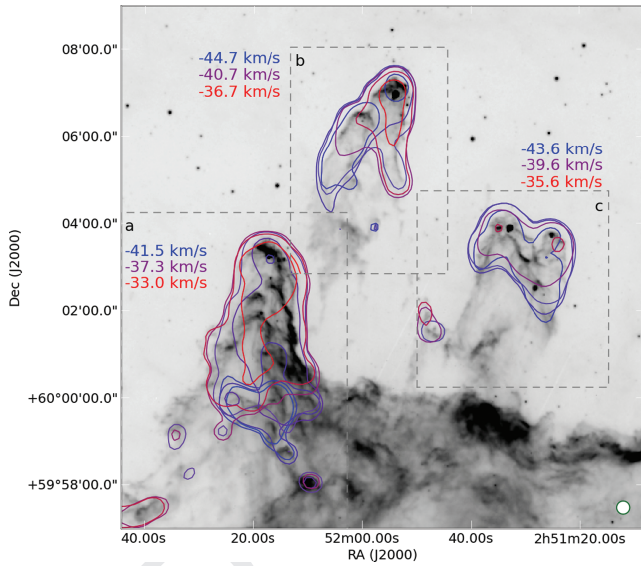


**Figure 19.** CO 3–2 contours overlaid on the *Spitzer* 8  $\mu$ m image of the W5S cometary clouds described in Section 4.4. Contours are colour-coded by velocity and shown for 0.84 km s $^{-1}$  channels at levels of 1 K (a, b) and 0.5 K (c). The velocity ranges plotted are (a)  $-41.5$  to  $-33.0$  km s $^{-1}$ , (b)  $-44.7$  to  $-36.7$  km s $^{-1}$ , (c)  $-43.6$  to  $-35.6$  km s $^{-1}$ . The labels show the minimum, maximum and middle velocities to guide the eye. The grey boxes indicate the regions selected for CO contours; while there is CO emission associated with the southern 8  $\mu$ m emission, we do not display it here. The velocity gradients are discussed in Section 4.4.

#### 4.5 W5 southeast

The region identified as W5SE has very little star formation activity despite having significant molecular gas ( $M_{^{13}\text{CO}} \sim 800 M_\odot$ ). While there are two outflows and two Class I objects (Koenig et al. 2008) in the southeast of the two clumps ( $\ell = 138.15, b = 0.77$ , Fig. 20), the main clump ( $\ell = 138.0, b = 0.8$ ) has no detected outflows. The CO emission is particularly clumpy in this region, with many independent, unresolved clumps both in position and in velocity. In the 8 and 24  $\mu$ m *Spitzer* images, it is clear that these clouds are illuminated from the north-west. This region represents a case in which the expanding H<sub>II</sub> region has impacted molecular gas but has not triggered additional star formation. The high clump-to-clump velocity dispersion observed in this region may be analogous to the W5S cometary clouds (Section 4.4) but without condensed clumps around which to form cometary clouds.

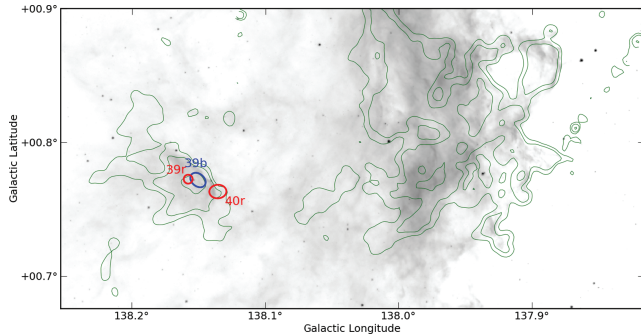


**Figure 20.** Small-scale map of the W5 SE region showing the star-forming clump containing outflows 39 and 40 and the non-star-forming clump at  $\ell = 138.0, b = 0.8$ . CO 3–2 contours integrated from  $-60$  to  $-20$  km s $^{-1}$  are displayed at levels 3, 7.2, 17.3, 41.6 and 100 K km s $^{-1}$ .

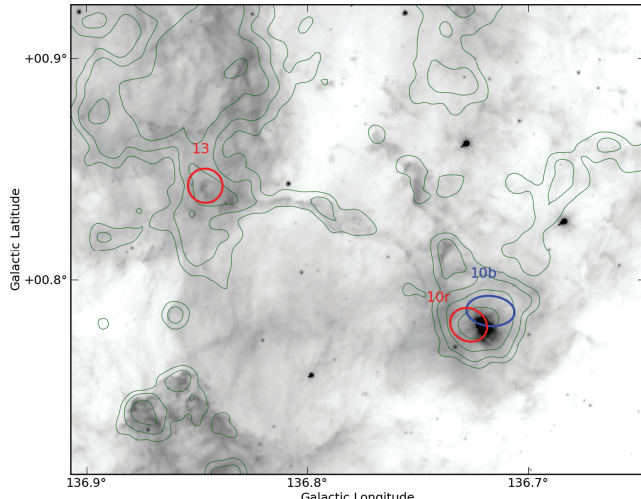


**Figure 21.** Small-scale map of the W5 SW region plotted with CO 3–2 contours integrated from  $-60$  to  $-20 \text{ km s}^{-1}$  at levels 3, 7.2, 17.3, 41.6 and  $100 \text{ K km s}^{-1}$ . Outflow 13 is at the head of a cometary cloud (Fig. 22) and therefore has clearly been affected by the expanding H II region, but the region including bipolar Outflow 10 shows no evidence of interaction with the H II region.

#### 4.6 W5 southwest

There is an isolated clump associated with outflows in the southwest part of W5 (Fig. 21) at  $v_{\text{LSR}} \sim -45 \text{ km s}^{-1}$ . While this clump is likely to be associated with the W5 region, it shows little evidence of interaction with the H II region. If it is eventually impacted by the expanding ionization front (i.e. if it is within the W5 complex), this clump will be an example of ‘revealed’, not triggered, star formation.

The other source in W5SW is a cometary cloud with a blueshifted head and redshifted tail (Fig. 22; Outflow 13). The head contains a redshifted outflow; no blueshifted counterpart was detected (the velocity gradient displayed in Fig. 22 is smaller than the outflow

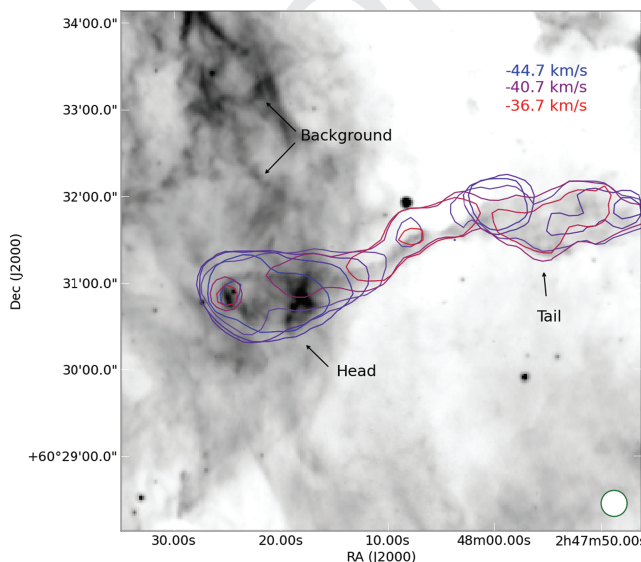


**Figure 22.** The cometary cloud in the W5 Southwest region (Outflow 13). Contours are shown at 1 K for  $0.84 \text{ km s}^{-1}$  wide channels from  $-37.2 \text{ km s}^{-1}$  (blue) to  $-30.5 \text{ km s}^{-1}$  (red). The head is clearly blueshifted relative to the tail and contains a spatially unresolved redshifted outflow.

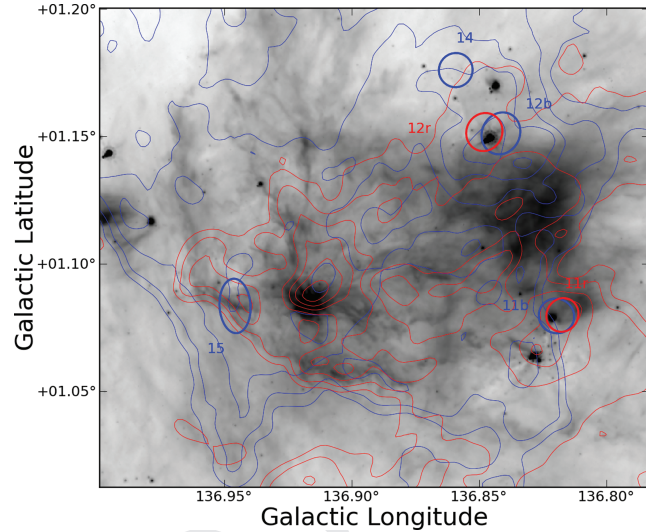


**Figure 23.** Small-scale map of the W5 W region. The IRAC 8  $\mu\text{m}$  image is displayed in inverted log scale from 800 to 8000 MJy  $\text{sr}^{-1}$ . Contours of the CO 3–2 cube integrated from  $-50$  to  $-38 \text{ km s}^{-1}$  (blue) and  $-38$  to  $-26 \text{ km s}^{-1}$  (red) are overlaid at levels 5, 10, 20, 30, 40, 50, 60 K  $\text{km s}^{-1}$   $\sigma \approx 0.5 \text{ K km s}^{-1}$ . The lack of outflow detections is partly explained by the two spatially overlapping clouds that are adjacent in velocity.

velocity and is also redshifted away from the head). The lack of a blueshifted counterpart may be because the flow is blowing into ionized gas where the CO is dissociated.

Because of its evident interaction with the H II region, this source is an interesting candidate for a non-protostellar outflow impersonator. However, because the head is blueshifted relative to the tail, we can infer that the head has been accelerated towards us by pressure from the H II region, implying that it is in the foreground of the cloud. Given this geometry, a radiation-driven flow would appear blueshifted, not redshifted, as the detected flow is. Additionally, the outflow is seen as fast as  $7.5 \text{ km s}^{-1}$  redshifted from the cloud, which is a factor of 2 too fast to be driven by radiation in a standard D-type shock. Finally, the outflow velocity is much greater than seen in a simulation of a cometary cloud by Gritschneider et al. (2010), while the head-to-tail velocity gradient is comparable.

#### 4.7 W5 West/IC 1848

There is a bright infrared source seen in the centre of W5W (IRAS 02459+6029; Fig. 23), but the nearest CO outflow lobe is  $\approx 1 \text{ pc}$  away. The non-detection may be due to confusion in this area: there are two layers of CO gas separated by  $\sim 5 \text{ km s}^{-1}$ , so low-velocity outflow detection is more difficult. Unlike the rest of the W5 complex, this region appears to have multiple independent confusing components along the line of sight (Fig. 13), and therefore the CO data provide much less useful physical information (multiple components are also observed in the  $^{13}\text{CO}$  data, ruling out self-absorption as the cause of the multiple components).

#### 4.8 W5 NW

The north-west cluster containing outflows 1–8 is at a slightly different velocity ( $\sim -35 \text{ km s}^{-1}$ ) than the majority of the W5 cloud complex ( $\sim -38 \text{ km s}^{-1}$ ; Fig. 24), but it shares contiguous emission with the neighbouring W5W region. It contains many outflows and therefore is actively forming stars (Fig. 25). However, this cluster

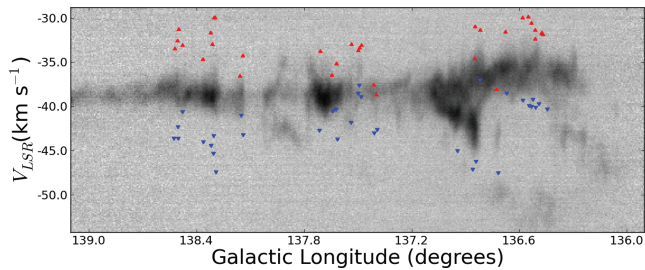


**Figure 24.** Integrated longitude–velocity diagram of the W5 complex from  $b = 0.25$  to  $b = 2.15$  in  $^{12}\text{CO}$  1–0 from the FCRAO OGS. The W5NW region is seen at a distinct average velocity around  $\ell = 136.5$ ,  $v_{\text{LSR}} = -34 \text{ km s}^{-1}$ . The red and blue triangles mark the longitude–velocity locations of the detected outflows. In all cases, they mark the low-velocity start of the outflow.

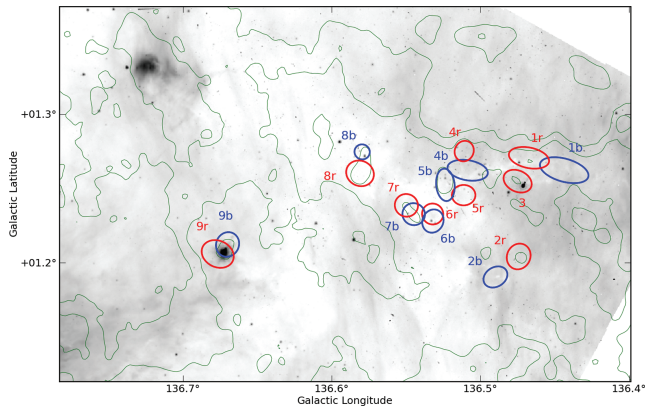


**Figure 25.** Small-scale map of the W5 NW region plotted with CO 3–2 contours integrated from  $-60$  to  $-20 \text{ km s}^{-1}$  at levels 3, 7.2, 17.3, 41.6 and  $100 \text{ K km s}^{-1}$ . Despite its distance from the W5 O-stars,  $D_{\text{proj}} \approx 20 \text{ pc}$ , this cluster is the most active site of star formation in the complex as measured by outflow activity.

exhibits much lower CO brightness temperatures and weaker *Spitzer* 8  $\mu\text{m}$  emission than the ‘bright-rimmed clouds’ seen near the W5 O-stars. We therefore conclude that the region has not been directly impacted by any photoionizing radiation from the W5 O-stars.

The lack of interaction with the W5 O-stars implies that the star formation in this region, though quite vigorous, has not been directly triggered. Therefore, not all of the current generation of star formation in W5 has been triggered on small or intermediate scales (e.g. radiation-driven implosion). Even the ‘collect and collapse’ scenario seems unlikely here, as the region with the most outflows also displays some of the smoothest morphology (Figs 2 and 25); in ‘collect and collapse’ the expansion of an HII region leads to clumping and fragmentation, and the spaces between the clumps should be relatively cleared out.

## 5 DISCUSSION

### 5.1 Comparison to other outflows

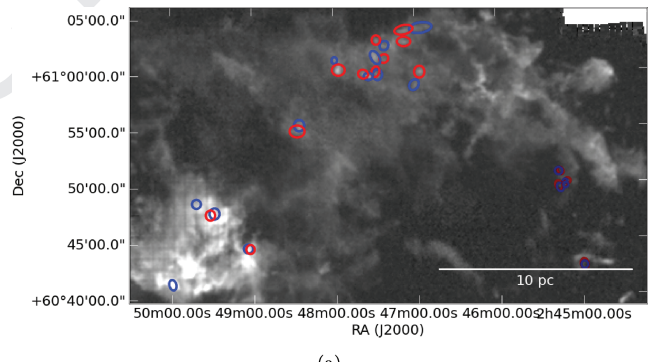
The outflow properties we derive are similar to those in the B0-star-forming clump IRAS 05358+3543 ( $M \approx 600 M_{\odot}$ ; Ginsburg et al. 2009), in which CO 3–2 and 2–1 were used to derive outflow masses in the range  $0.01$ – $0.09 M_{\odot}$ . However, some significantly larger outflows, up to 1.6 pc in one direction, were detected, while

the largest resolved outflow in our survey was only 0.8 pc (one direction).

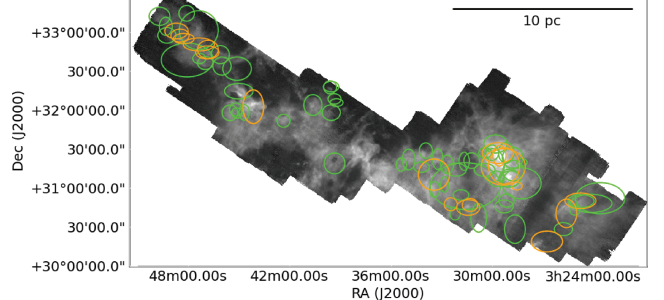
As noted in Section 3.1.1, the total molecular mass in W5 is larger than Perseus,  $M_{\text{W5}} \sim 4.5 \times 10^4 M_{\odot}$  while  $M_{\text{Perseus}} \sim 10^4 M_{\odot}$  (Bally et al. 2008). The length distribution of outflows (Fig. 8) is strikingly similar, while other physical properties have substantially different mean values with or without correction factors included.

The W5NW region is more directly comparable to Perseus, with a total mass of  $\sim 1.5 \times 10^4 M_{\odot}$  (Table 1) and a similar size. In Fig. 3, we show both the W5NW region, which contains all of the identified outflows, and the W5NWpc region, which is a larger area intended to be directly comparable in both mass and spatial scale to the Perseus molecular cloud. The W5NWpc region contains more than an order of magnitude more turbulent energy than the Perseus complex ( $E_{\text{turb,Per}} = 1.6 \times 10^{46} \text{ erg}$ ; Arce et al. 2010) despite its similar mass. Even the smaller W5NW region has nearly five times more turbulent energy than the Perseus complex, largely because of the greater average linewidth ( $\sigma_{\text{FWHM,W5NW}} \approx 3.5 \text{ km s}^{-1}$ ). As with the whole of W5, there is far too much turbulent energy in W5NW to be provided by outflows alone, implying the presence of another driver of turbulence.

Fig. 26 shows the W5NWpc region and Perseus molecular cloud on the same scale, though in two different emission lines. The Perseus cloud contains many more outflows and candidates (70 in Perseus versus 13 in W5NWpc) despite a much larger physical area



(a)



(b)

**Figure 26.** (a) An integrated CO 3–2 image of the W5W/NW region with ellipses overlaid displaying the locations and sizes of outflows. The dark red and blue ellipses in the lower right are associated with outer-arm outflows. W5W is the bottom-left, CO-bright region. W5NW is the top-centre region containing the cluster of outflows. (b) An integrated CO 1–0 image of the Perseus molecular cloud from the COMPLETE survey (Arce et al. 2010). Note that the spatial scale is identical to that of (a) assuming that W5 is eight times more distant than Perseus. The green ellipses represent Arce et al. (2010) CPOCs while the orange represent known outflows from the same paper.

surveyed in W5. While it is likely that many of the W5W outflows will break apart into multiple flows at higher resolution, it does not seem likely that each would break apart into five flows, as would be required to bring the numbers into agreement. Since the highest density of outflows in Perseus is in the NGC 1333 cloud, it may be that there is no equivalently evolved region in W5NWpc. The W5W region may be comparably massive, but it is also confused and strongly interacting with the W5 H II region – either star formation is suppressed in this region or outflows are rendered undetectable. In the latter case, the most likely mechanisms for hiding outflows are molecular dissociation by ionizing radiation and velocity confusion.

Another possibility highlighted in Fig. 26 is that the W5NW region is interacting with the W4 bubble. The cloud in the top right of Fig. 26 is somewhat cometary, has higher peak brightness temperature and is at a slightly different velocity ( $-45 \text{ km s}^{-1}$ ) than W5NW. The velocity difference of  $\sim 8 \text{ km s}^{-1}$  could simply be two clouds physically unassociated along the line of sight, or could indicate the presence of another expanding bubble pushing two sheets of gas away from each other. Either way, the north-west portion of the W5NW region is clumpier than the area in which the outflows were detected, and it includes no outflow detections.

## 5.2 Star formation activity

CO outflows are an excellent tracer of ongoing embedded star formation (e.g. Shu, Adams & Lizano 1987). We use the locations of newly discovered outflows to qualitatively describe the star forma-

tion activity within the W5 complex and evaluate the hypothesis that star formation has been triggered on small or intermediate scales.

Class 0/I objects are nearly always associated with outflows in nearby star-forming regions (e.g. Hatchell et al. 2007; Perseus Curtis et al. 2010). However, Koenig et al. (2008) detected 171 Class I sources in W5 using *Spitzer* photometry. Since our detection threshold for outflow appears to be similar to that in Perseus (Section 3.1.1), the lower number of outflow detections is surprising, especially considering that some of the detected outflows are outside the *Spitzer*-MIPS field (MIPS detections are required for Class I objects, and flows 1–4 are outside that range) or are in the outer arm (flows 39–54). Additionally, we should detect outflows from Class 0 objects that would not be identified by *Spitzer* colours.

There are a number of explanations for our detection deficiency. The Class I objects detected within the H II region ‘bubble’ most likely have outflows in which the CO is dissociated similar to jet systems in Orion (e.g. HH46/47, a pc-scale flow in which CO is only visible very near the protostar; Chernin & Masson 1991; Stanke, McCaughrean & Zinnecker 1999). This hypothesis can be tested by searching for optical and infrared jets associated with these objects, which presumably have lower mass envelopes and therefore less extinction than typical Class I objects. Additionally, there are many outflow systems that are likely to be associated with clusters of outflows rather than individual outflows as demonstrated in Section 3.1.1, where we were able to identify fewer outflows when ‘observing’ the Perseus objects at a greater distance. There are 24 sources in the Koenig et al. (2008) Class I catalogue within 15 arcsec (one JCMT beam at 345 GHz) of another, and in many cases there

**Table 4.** Outer arm CO 3–2 outflows – measured properties.

Outflow number	Latitude	Longitude	Ellipse major (arcsec)	Ellipse minor (arcsec)	Ellipse PA (°)	Kinematic distance (pc)	$R_G^a$ (pc)	Velocity centre ( $\text{km s}^{-1}$ )	Velocity min	Velocity max	$\int T_A^* dv$ (K $\text{km s}^{-1}$ )
41r	136.364	0.9606	25	18	2	5510	13 000	-61.8	-59.2	-56.5	0.5
41b	136.3634	0.9568	23	17	353	5510	13 000	-61.8	-71.6	-64.3	3.0
42r	136.3522	0.9786	20	14	2	5500	12 900	-62.1	-59.8	-57.6	0.6
42b	136.3548	0.9798	20	19	332	5500	12 900	-62.1	-67.8	-64.4	0.5
43r	136.3495	0.9612	17	15	63	5510	13 000	-61.8	-59.0	-56.1	0.8
43b	136.353	0.9621	12	12	333	5510	13 000	-61.8	-66.3	-64.6	1.0
44r	136.3554	0.9576	13	13	23	5500	12 900	-61.8	-59.0	-55.4	2.1
44b	136.3545	0.9567	14	14	333	5500	12 900	-61.8	-68.0	-64.5	2.0
45r	136.1219	2.0816	34	25	297	3750	11 400	-46.5	-43.1	-40.5	0.6
45b	136.1233	2.0803	35	25	306	3750	11 400	-46.5	-57.3	-50.0	1.9
46	136.1166	2.0983	26	25	332	3790	11 400	-50.2	-52.6	-50.2	0.5
47b	136.3857	2.2687	34	27	332	3220	11 000	-42.0	-55.0	-46.7	3.5
47r	136.3861	2.267	35	23	304	3220	11 000	-42.0	-37.3	-25.1	5.0
48b	136.374	2.2628	29	21	332	3250	11 000	-43.2	-51.4	-47.0	1.5
48r	136.3736	2.2615	29	22	332	3250	11 000	-43.2	-39.5	-22.2	8.9
49r	136.4663	2.4678	29	23	290	3610	11 300	-45.7	-42.2	-33.0	2.2
49b	136.4661	2.4693	31	23	292	3610	11 300	-45.7	-52.2	-49.1	0.9
50b	136.5087	2.5108	31	25	332	3380	11 100	-43.5	-48.5	-46.5	0.8
50r	136.5118	2.5083	28	23	10	3380	11 100	-43.5	-40.6	-37.5	1.0
51b	137.058	2.9858	28	23	293	4350	11 900	-51.8	-55.5	-53.0	0.8
51r	137.0567	2.9864	34	25	8	4350	11 900	-51.8	-50.6	-40.9	3.5
52r	137.0662	2.9999	37	26	43	4390	12 000	-52.2	-49.1	-41.0	7.8
52b	137.0683	3.0013	38	29	15	4390	12 000	-52.2	-65.8	-55.2	4.1
53b	138.6143	1.5611	26	26	330	5450	13 000	-59.7	-71.1	-61.7	5.5
53r	138.6158	1.563	25	23	330	5450	13 000	-59.7	-57.6	-54.5	1.3
54r	136.382	0.8392	29	20	343	7480	14 700	-75.6	-73.2	-68.9	2.6
54b	136.3824	0.838	20	17	332	7480	14 700	-75.6	-83.1	-77.9	2.0
55b	136.7623	0.4548	27	16	343	5230	12 700	-60.9	-65.2	-62.7	5.4
55r	136.7579	0.4522	24	18	343	5230	12 700	-60.9	-59.0	-53.2	6.0

<sup>a</sup>Galactocentric radius.

3 are multiple Koenig et al. (2008) Class I sources within the contours  
4 of a single outflow system.

### 5 6 7 5.3 Evaluating triggering

8 In the previous section, we discussed in detail the relationship  
9 between each sub-region and the H $\alpha$  region. Some regions are ob-  
10 served to be star forming but not interacting with the H $\alpha$  region  
11 (W5NW, Sh 2-201), while others are interacting with the H $\alpha$  re-  
12 gion but show no evidence or reduced evidence of star formation  
13 (W5SE, W5W, LW Cas). At the very least, there is significant com-  
14 plexity in the triggering mechanisms, and no one mechanism or size  
15 scale is dominant. If we were to trust outflows as unbiased tracers  
16 of star formation, we might conclude that the majority of star for-  
17 mation in W5 is untriggered (spontaneous), but such a conclusion  
18 is unreliable because both radiatively triggered star formation and  
19 ‘revealed’ star formation may not exhibit molecular outflows (al-  
20 though ionized atomic outflows should still be visible around young  
21 stars formed through these scenarios).

22 In Section 4.3, we analysed a particular case in which the RDI  
23 mechanism could plausibly have crushed a cloud to create the ob-  
24 served protostar. It is not possible to determine whether interaction  
25 with the H $\alpha$  region was a necessary precondition for the star’s for-  
26 mation, but it at least accelerated the process. The other cometary  
27 clouds share this property, but in total there are only five cometary  
28 clouds with detected outflows at their tips, indicating that this mech-  
29 anism is not the dominant driver of star formation in W5.

30 The ‘collect and collapse’ scenario might naively be expected  
31 to produce an excess of young stars at the interaction front be-  
32 tween the H $\alpha$  region and the molecular cloud. However, because  
33 such interactions naturally tend to form instabilities, this scenario  
34 produces cloud morphologies indistinguishable from those of RDI.  
35 There is not an obvious excess of sources associated with cloud  
36 edges over those deep within the clouds (e.g. Fig. 2). We therefore  
37 cannot provide any direct evidence for this triggering scenario.

38 The overall picture of W5 is of two concurrent episodes of mas-  
39 sive star formation that have led to adjacent blown-out bubbles.  
40 Despite the added external pressure along the central ridge, it is  
41 relatively deficient in both star formation activity and dense gas,  
42 perhaps because of heating by the strong ionizing radiation field.  
43 The lack of star formation along that central ridge implies that much  
44 of the gas was squeezed and heated, but it was not crushed into grav-  
45 itationally unstable fragments. While some star formation may have  
46 been triggered in W5, there is strong evidence for pre-existing star  
47 formation being at least a comparable, if not the dominant, mech-  
48 anism of star formation in the complex.

## 51 52 53 54 55 56 57 58 59 60 61 62 63 64 6 OUTFLOW SYSTEMS BEYOND W5

65 Fifteen outflows were detected at velocities inconsistent with the  
66 local W5 cloud velocities. Of these, eight are consistent with Perseus  
67 arm velocities ( $v_{\text{LSR}} > -55 \text{ km s}^{-1}$ ) and could be associated with  
68 different clouds within the same spiral arm. The other seven have  
69 central velocities  $v_{\text{LSR}} < -55 \text{ km s}^{-1}$  and are associated with the  
70 outer arm identified in previous surveys (e.g. Digel et al. 1996).  
71 The properties of these outflows are given in Tables 4 and 5; the  
72 distances listed are kinematic distances assuming  $R_0 = 8.4 \text{ kpc}$  and  
73  $v_0 = 254 \text{ km s}^{-1}$  (Reid et al. 2009).

74 Of these outflows, all but one are within 2 arcmin of an IRAS  
75 point source. Outflow 54 is the most distant in our survey at a  
76 kinematic distance  $d = 7.5 \text{ kpc}$  ( $v_{\text{LSR}} = -75.6 \text{ km s}^{-1}$ ) and galac-

Table 5. Outer arm CO 3–2 outflows – derived properties.

Outflow number	Mass ( $M_\odot$ )	Momentum ( $M_\odot \text{ km s}^{-1}$ )	Energy ( $10^{42} \text{ erg}$ )	Dynamical age ( $10^4 \text{ yr}$ )	Momentum flux ( $10^{-6} M_\odot \text{ km s}^{-1} \text{ yr}^{-1}$ )
41r	0.037	0.11	3.5	3.6	30.2
41b	0.196	0.96	54.6	3.6	30.2
42r	0.029	0.06	1.3	4.3	3.9
42b	0.03	0.11	3.9	4.3	3.9
43r	0.033	0.13	5.1	7.3	2.9
43b	0.024	0.08	2.8	7.3	2.9
44r	0.062	0.21	7.9	1.8	27.7
44b	0.067	0.28	12.6	1.8	27.7
45r	0.037	0.18	8.6	1.2	62.3
45b	0.126	0.55	28.3	1.2	62.3
46	0.028	0.1	3.7	–	–
47b	0.187	1.32	101.0	0.6	553.0
47r	0.232	1.84	164.0	0.6	553.0
48b	0.054	0.33	20.8	0.4	754.0
48r	0.341	2.4	229.0	0.4	754.0
49r	0.106	0.77	62.7	1.4	71.1
49b	0.047	0.22	10.8	1.4	71.1
50b	0.037	0.14	5.5	3.8	7.4
50r	0.038	0.14	5.5	3.8	7.4
51b	0.058	0.13	3.0	1.0	152.0
51r	0.303	1.33	72.7	1.0	152.0
52r	0.829	4.3	250.0	1.4	479.0
52b	0.472	2.5	150.0	1.4	479.0
53b	0.626	3.16	194.0	4.7	73.2
53r	0.124	0.31	8.5	4.7	73.2
54r	0.461	1.24	37.5	1.8	135.0
54b	0.212	1.14	64.0	1.8	135.0
55b	0.411	1.66	68.0	7.5	28.3
55r	0.404	0.47	6.6	7.5	28.3

tocentric distance  $D_G = 14.7 \text{ kpc}$ . It has no known associations in the literature.

Outflows 41–44 are associated with a cloud at  $v_{\text{LSR}} \sim -62 \text{ km s}^{-1}$  known in the literature as LDN 1375 and associated with IRAS 02413+6037. Outflows 53 and 55 are at a similar velocity and associated with IRAS 02598+6008 and IRAS 02425+6000, respectively. All of these sources lie roughly on the periphery of the W5 complex.

Outflows 45–52 are associated with a string of IRAS sources and H $\alpha$  regions to the north of W5 and have velocities in the range  $-55 < v_{\text{LSR}} < -45$ . They therefore could be in the Perseus arm but are clearly unassociated with the W5 complex. Outflows 45 and 46 are associated with IRAS 02435+6144 and they may also be associated with the Sharpless H $\alpha$  region Sh 2-194. Outflows 47 and 48 are associated with IRAS 02461+6147, also known as AFGL 5085. Outflows 49 and 50 are nearby but not necessarily associated with IRAS 02475+6156, and may be associated with Sh 2-196. Outflows 51 and 52 are associated with IRAS 02541+6208.

## 7 CONCLUSIONS

We have identified 40 molecular outflow candidates in the W5 star-forming region and an additional 15 outflows spatially coincident but located in the outer arm of the Galaxy.

(i) The majority of the CO clouds in the W5 complex are forming stars. Star formation is not limited to cloud edges around the H $\alpha$  region. Because star formation activity is observed outside of

the region of influence of the W5 O-stars, it is apparent that direct triggering by massive star feedback is not responsible for all of the star formation in W5.

(ii) The W5 complex is seen nearly face-on as evidenced by a strict upper limit on the CO column through the centre of the H $\text{II}$ -region bubbles. It is therefore an excellent region to study massive star feedback and revealed and triggered star formation.

(iii) Outflows contribute negligibly to the turbulent energy of molecular clouds in the W5 complex. This result is unsurprising near an H $\text{II}$  region, but supports the idea that massive star-forming regions are qualitatively different from low-mass star-forming regions in which the observed turbulence could be driven by outflow feedback. Even in regions far separated from the O-stars, there is more turbulence and less energy injection from outflows than in, e.g., Perseus.

(iv) Despite detecting a significant number of powerful outflows, the total outflowing mass detected in this survey ( $\sim 1.5 \text{ M}_\odot$  without optical depth correction, perhaps  $10\text{--}20 \text{ M}_\odot$  when optical depth is considered) was somewhat smaller than in Perseus, a low- to intermediate-mass star-forming region with  $\sim 1/6$  the molecular mass of W5.

(v) The low mass measured may be partly because the CO 3–2 line is sub-thermally excited in outflows. Therefore, while CO 3–2 is an excellent tracer of outflows for detection, it does not serve as a ‘calorimeter’ in the same capacity as CO 1–0.

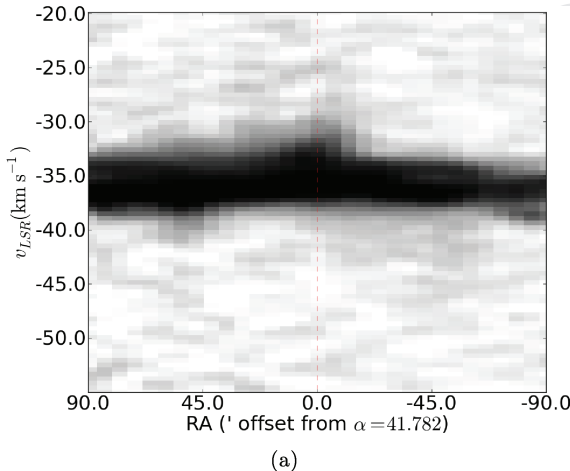
(vi) Even considering excitation and optical depth corrections, it is likely that the mass of outflows in W5 is less than would be expected from a simple extrapolation from Perseus based on cloud mass. CO is likely to be photodissociated in the outflows when they reach the H $\text{II}$  region, accounting for the deficiency around the H $\text{II}$  region edges. However, in areas unaffected by the W5 O-stars such as W5NW, the deficiency may be because the greater turbulence in the W5 clouds suppresses star formation or hides outflows.

(vii) Velocity gradients across the tails of many cometary clouds have been observed, hinting at their geometry and confirming that the outflows seen from their heads must be generated by protostars within.

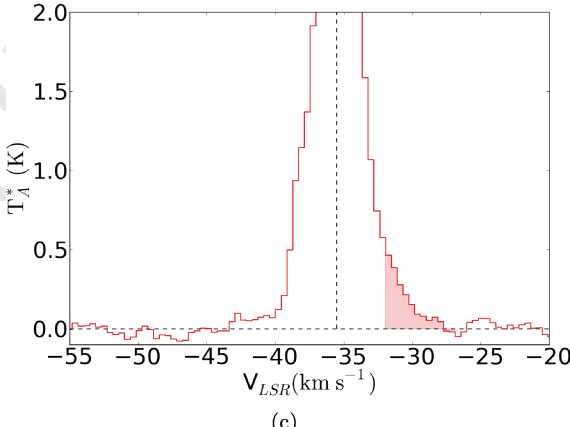
(viii) Outflows have been detected in the Outer Arm at galactocentric distances  $\gtrsim 12 \text{ kpc}$ . These represent some of the highest galactocentric distance star-forming regions discovered to date.

## 8 ONLINE-ONLY MATERIAL

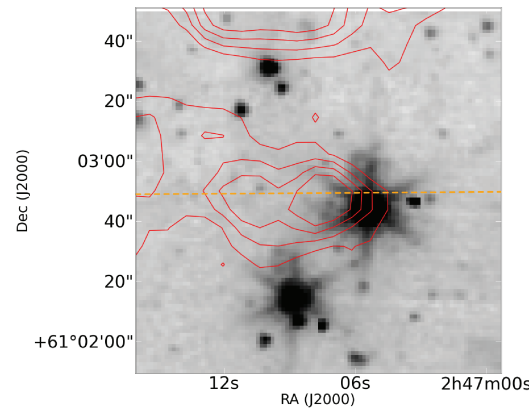
As Supporting Information with the online version of the article, we present position–velocity diagrams, contour overlays on infrared images and integrated spectra for all of the outflows identified in the survey. An example is presented here as Fig. 27. The overlays are on *Spitzer* 4.5  $\mu\text{m}$  and 8  $\mu\text{m}$  images except where otherwise noted; the exceptions are because the CO 3–2 survey covered a larger area than the *Spitzer* survey. The contours are displayed at levels 0.5, 1,



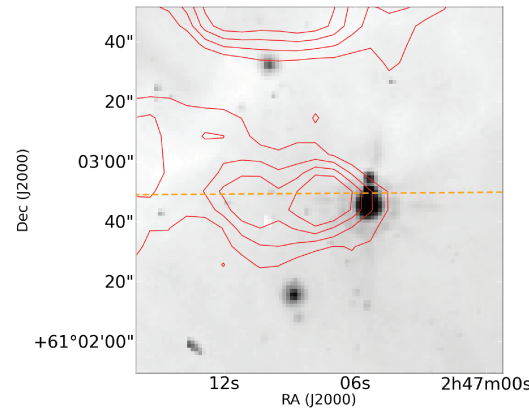
(a)



(c)



(b)



(d)

**Figure 27.** Position–velocity diagrams, spectra and contour overlays of Outflow 3. No blue counterpart to this flow was identified, although it is possible that the blue lobe in Outflow 4 is actually associated with this source. Additional figures for all other outflows are available in the online version (see Supporting Information).

1.5, 2, 3, 4, 5, 6 K km s<sup>-1</sup> except where otherwise noted. The typical noise level in the contoured CO maps is  $\sigma \approx 0.25$  K km s<sup>-1</sup>.

## ACKNOWLEDGMENTS

We thank the two anonymous referees for their assistance in refining this document. We thank Devin Silvia for a careful proof-reading of the text. This work has made use of the APLpy plotting package (<http://aplpy.sourceforge.net>), the PYREGION package (<http://leejjoon.github.com/pyregion/>), the AGPY code package (<http://code.google.com/p/agpy/>), IPAC's Montage (<http://montage.ipac.caltech.edu/>), the DS9 visualization tool (<http://hea-www.harvard.edu/RD/ds9/>), the pyspeckit spectroscopic analysis toolkit (<http://pyspeckit.bitbucket.org>) and the STARLINK package (<http://starlink.jach.hawaii.edu/>). *IRAS* data were acquired through IRSA at IPAC (<http://irsa.ipac.caltech.edu/>). DRAO 21 cm data were acquired from the Canadian Astronomical Data Center (<http://cadcwww.hia.nrc.ca/cgps/>). The authors are supported by the National Science Foundation through NSF grant AST-0708403. This research has made use of the SIMBAD data base, operated at CDS, Strasbourg, France.

Facilities: JCMT, VLA

Q25

## REFERENCES

- Adams F. C., Fatuzzo M., 1996, ApJ, 464, 256  
 Arce H. G., Borkin M. A., Goodman A. A., Pineda J. E., Halle M. W., 2010, ApJ, 715, 1170  
 Bachiller R., 1996, ARA&A, 34, 111  
 Bally J., Walawender J., Johnstone D., Kirk H., Goodman A., 2008, Reipurth B., ed., The Perseus Cloud, p. 308  
 Beaumont C. N., Williams J. P., 2010, ApJ, 709, 791  
 Bertoldi F., McKee C. F., 1990, ApJ, 354, 529  
 Bourke T. L. et al., 1997, ApJ, 476, 781  
 Bretherton D. E., Moore T. J. T., Ridge N. A., 2002, Hot Star Workshop III: The Earliest Phases of Massive Star Birth, Vol. 267, p. 347  
 Cabrit S., Bertout C., 1990, ApJ, 348, 530  
 Chernin L. M., Masson C. R., 1991, ApJ, 382, L93  
 Curtis E. I., Richer J. S., Swift J. J., Williams J. P., 2010, MNRAS, 1304  
 Cyganowski C. J., Brogan C. L., Hunter T. R., Churchwell E., 2009, ApJ, 702, 1615
- Deharveng L., Zavagno A., Cruz-Gonzalez I., Salas L., Caplan J., Carrasco L., 1997, A&A, 317, 459  
 Digel S. W., Lyder D. A., Philbrick A. J., Puche D., Thaddeus P., 1996, ApJ, 458, 561  
 Elmegreen B. G., 1998, in Woodward C. E., Shull J. M., Thronson H. A., Jr, eds, ASP Conf. Ser. Vol. 148, Origins. Astron Soc. Pac., San Francisco, p. 150  
 Elmegreen B. G., Lada C. J., 1977, ApJ, 214, 725  
 Enoch M. L. et al., 2006, ApJ, 638, 293  
 Evans N. J. et al., 2009, ApJS, 181, 321  
 Felli M., Hjellming R. M., Cesaroni R., 1987, A&A, 182, 313  
 Garden R. P., Hayashi M., Hasegawa T., Gatley I., Kaifu N., 1991, ApJ, 374, 540  
 Ginsburg A. G., Bally J., Yan C., Williams J. P., 2009, ApJ, 707, 310  
 Goldsmith P. F., 1972, ApJ, 176, 597  
 Gritschneider M., Burkert A., Naab T., Walch S., 2010, ApJ, 723, 971  
 Hachisuka K. et al., 2006, ApJ, 645, 337  
 Hatchell J., Dunham M. M., 2009, 0904.1163  
 Hatchell J., Fuller G. A., Richer J. S., 2007, A&A, 472, 187  
 Heyer M. H., Brunt C., Snell R. L., Howe J. E., Schloerb F. P., Carpenter J. M., 1998, ApJS, 115, 241  
 Karr J. L., Martin P. G., 2003, ApJ, 595, 900  
 Klein R. I., Sandford M. T., II, Whitaker R. W., 1983, ApJ, 271, L69  
 Koenig X. P., Allen L. E., Gutermuth R. A., Hora J. L., Brunt C. M., Muzerolle J., 2008, ApJ, 688, 1142  
 Lada C. J., Fich M., 1996, ApJ, 459, 638  
 Lefloch B., Lazareff B., Castets A., 1997, A&A, 324, 249  
 Muenter J., 1975, J. Molecular Spectroscopy, 55, 490 [is always cited for  $\mu = 0.122$  debye.]  
 Oey M. S., Watson A. M., Kern K., Walth G. L., 2005, AJ, 129, 393  
 Peters T., Banerjee R., Klessen R. S., Low M. M., Galván-Madrid R., Keto E. R., 2010, ApJ, 711, 1017  
 Reid M. J. et al., 2009, preprint (arXiv e-prints)  
 Reipurth B., Bally J., 2001, ARA&A, 39, 403  
 Shu F. H., Adams F. C., Lizano S., 1987, ARA&A, 25, 23  
 Snell R. L., Carpenter J. M., Heyer M. H., 2002, ApJ, 578, 229  
 Stanke T., McCaughrean M. J., Zinnecker H., 1999, A&A, 350, L43  
 Taylor A. R. et al., 2003, AJ, 125, 3145  
 Thompson M. A., White G. J., Morgan L. K., Miao J., Fridlund C. V. M., Huldtgren-White M., 2004, A&A, 414, 1017  
 van der Tak F. F. S., Black J. H., Schöier F. L., Jansen D. J., van Dishoeck E. F., 2007, A&A, 468, 627  
 Wilson T. L., Rohlfs K., Hüttemeister S., 2009, Tools of Radio Astronomy. Springer

Q31  
Q32

Q33  
Q34

Q35

Q36

Q37

Q38

## APPENDIX A: OPTICALLY THIN, LTE DIPOLE MOLECULE

While many authors have solved the problem of converting CO 1–0 beam temperatures to H<sub>2</sub> column densities (Cabrit & Bertout 1990; Garden et al. 1991; Lada & Fich 1996; Bourke et al. 1997), there are no examples in the literature of a full derivation of the LTE, optically thin CO-to-H<sub>2</sub> conversion process for higher rotational states. We present the full derivation here, and quantify the systematic errors generated by various assumptions.

We begin with the assumption of an optically thin cloud such that the radiative transfer equation (Wilson, Rohlfs & Hüttemeister 2009, equation 1.9) simplifies to

$$\frac{dI_v}{ds} = -\kappa_v I_v. \quad (\text{A1})$$

The absorption and stimulated emission terms yield

$$\kappa_v = \frac{h\nu_{ul}B_{ul}n_u}{c}\varphi(v) - \frac{h\nu_{ul}B_{lu}n_l}{c}\varphi(v), \quad (\text{A2})$$

where  $\varphi(v)$  is the line shape function ( $\int \varphi(v) dv \equiv 1$ ),  $n$  is the density in the given state,  $v$  is the frequency of the transition,  $B$  is the Einstein B coefficient and  $h$  is Planck's constant.

By assuming LTE (the Boltzmann distribution) and using Kirchoff's law and the definition of the Einstein A and B values, we can derive a more useful version of this equation

$$\kappa_v = \frac{c^2}{8\pi\nu_{ul}^2} n_u A_{ul} \left[ \exp\left(\frac{h\nu_{ul}}{k_B T_{ex}}\right) - 1 \right] \varphi(v) \quad (\text{A3})$$

where  $k_B$  is Boltzmann's constant.

The observable  $T_B$  can be related to the optical depth, which is given by

$$\int \tau_v dv = \frac{c^2}{8\pi\nu_{ul}^2} A_{ul} \left[ \exp\left(\frac{h\nu_{ul}}{k_B T_{ex}}\right) - 1 \right] \int \varphi(v) dv \int n_u ds. \quad (\text{A4})$$

Rearranging and converting from density to column ( $\int n ds = N$ ) give an equation for the column density of the molecule in the upper energy state of the transition:

$$N_u = \frac{8\pi\nu_{ul}^2}{c^2 A_{ul}} \left[ \exp\left(\frac{h\nu_{ul}}{k_B T_{ex}}\right) - 1 \right]^{-1} \int \tau_v dv. \quad (\text{A5})$$

In order to relate the brightness temperature to the optical depth, at CO transition frequencies the full blackbody formula must be used and the CMB must also be taken into account. Wilson et al. (2009) equation (15.29)

$$T_B(v) = \frac{h\nu}{k_B} \left( [e^{h\nu/k_B T_{ex}} - 1]^{-1} - [e^{h\nu/k_B T_{CMB}} - 1]^{-1} \right) (1 - e^{-\tau_v}) \quad (\text{A6})$$

is rearranged to solve for  $\tau_v$ :

$$\tau_v = -\ln \left[ 1 - \frac{k_B T_B}{h\nu} \left( [e^{h\nu/k_B T_{ex}} - 1]^{-1} - [e^{h\nu/k_B T_{CMB}} - 1]^{-1} \right)^{-1} \right]. \quad (\text{A7})$$

We convert from frequency to velocity units with  $dv = v/c dv$ , and plug (A7) into (A5) to get

$$N_u = \frac{8\pi\nu_{ul}^3}{c^3 A_{ul}} \left[ \exp\left(\frac{h\nu_{ul}}{k_B T_{ex}}\right) - 1 \right]^{-1} \int -\ln \left[ 1 - \frac{k_B T_B}{h\nu_{ul}} \left( [e^{h\nu_{ul}/k_B T_{ex}} - 1]^{-1} - [e^{h\nu_{ul}/k_B T_{CMB}} - 1]^{-1} \right)^{-1} \right] dv \quad (\text{A8})$$

which is the full LTE upper-level column density with no approximations applied.

The first term of the Taylor expansion is appropriate for  $\tau \ll 1$  ( $\ln[1+x] \approx x - \frac{x^2}{2} + \frac{x^3}{3} \dots$ )

$$N_u = \frac{8\pi\nu_{ul}^3}{c^3 A_{ul}} \left[ \exp\left(\frac{h\nu_{ul}}{k_B T_{ex}}\right) - 1 \right]^{-1} \int \frac{k_B T_B}{h\nu_{ul}} \left( [e^{h\nu_{ul}/k_B T_{ex}} - 1]^{-1} - [e^{h\nu_{ul}/k_B T_{CMB}} - 1]^{-1} \right)^{-1} dv \quad (\text{A9})$$

which simplifies to

$$N_u = \frac{8\pi\nu_{ul}^2 k_B}{c^3 A_{ul} h} \frac{e^{h\nu_{ul}/k_B T_{CMB}} - 1}{e^{h\nu_{ul}/k_B T_{CMB}} - e^{h\nu_{ul}/k_B T_{ex}}} \int T_B dv. \quad (\text{A10})$$

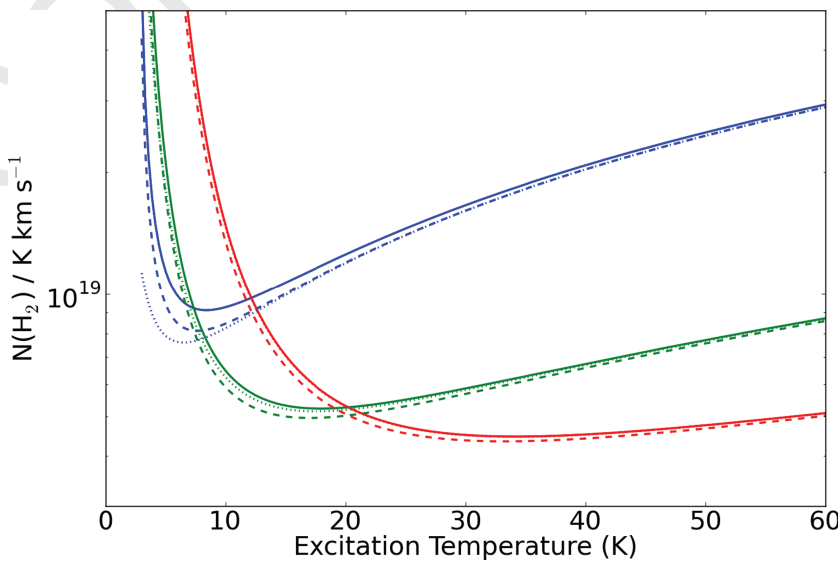


**Figure A1.** The LTE, optically thin conversion factor from  $T_B$  ( $\text{K km s}^{-1}$ ) to  $N(\text{H}_2)$  ( $\text{cm}^{-2}$ ) assuming  $X_{12}\text{CO} = 10^{-4}$  plotted against  $T_{ex}$ . The dashed line shows the effect of using the integral approximation of the partition function (e.g. Cabrit & Bertout 1990). It is a better approximation away from the critical point, and is a better approximation for higher transitions. The dotted line shows the effects of removing the CMB term from (A6); the CMB populates the lowest two excited states, but contributes nearly nothing to the  $J = 3$  state. Top (blue):  $J = 1-0$ , middle (green):  $J = 2-1$ , bottom (red):  $J = 3-2$ .

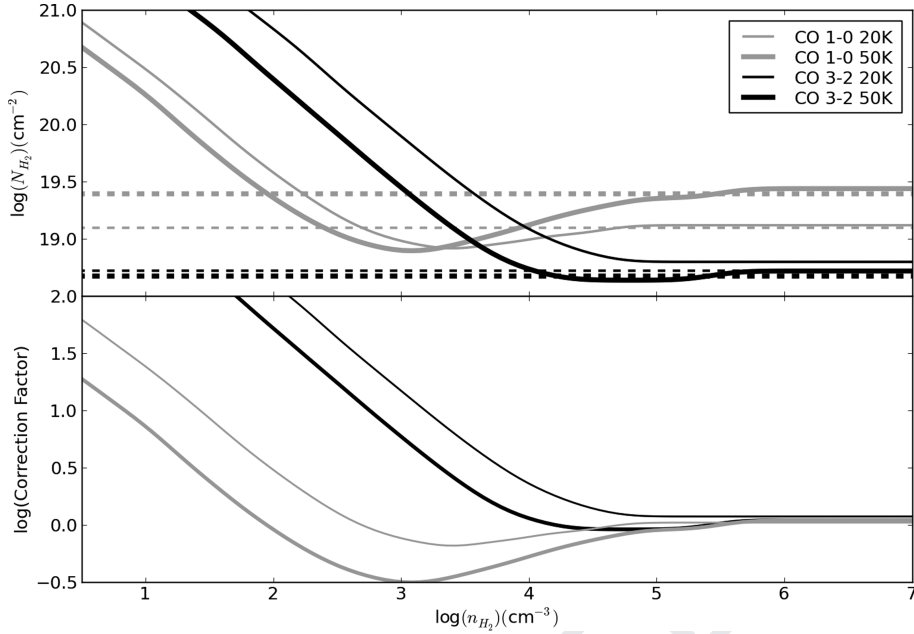


**Figure A2.** Top: the derived  $N(H_2)$  as a function of  $n_{H_2}$  for  $T_B = 1$  K. The dashed lines represent the LTE-derived  $N(H_2)/T_B$  factor, which has no density dependence and, for CO 3–2, only a weak dependence on temperature. We assume an abundance of  $^{12}\text{CO}$  relative to  $H_2$   $X_{\text{CO}} = 10^{-4}$ . Bottom: the correction factor  $[N(H_2)_{\text{RADEX}} / N(H_2)_{\text{LTE}}]$  as a function of  $n_{H_2}$ . For  $T_K = 20$  K, the ‘correction factor’ at  $10^3 \text{ cm}^{-3}$  (typical GMC mean volume densities) is  $\sim 15$ , while at  $10^4 \text{ cm}^{-3}$  (closer to  $n_{\text{crit}}$  but perhaps substantially higher than GMC densities) it becomes negligible. The correction factor is also systematically lower for a higher gas kinetic temperature. For some densities, the ‘correction factor’ dips below 1, particularly for CO 1–0. This effect is from a slight population inversion due to fast spontaneous decay rates from the higher levels and has been noted before (e.g. Goldsmith 1972).

This can be converted to use  $\mu_e$  (0.1222 for  $^{12}\text{CO}$ ; Muenker 1975), the electric dipole moment of the molecule, instead of  $A_{ul}$ , using Wilson et al. (2009) equation 15.20 ( $(A_{ul} = (64\pi^4)/(3hc^3)) v^3 \mu_e^2$ ):

$$N_u = \frac{3}{8\pi^3 \mu_e^2} \frac{k_B}{v_{ul}} \frac{2J_u + 1}{J_u} \frac{e^{hv_{ul}/k_B T_{\text{CMB}}} - 1}{e^{hv_{ul}/k_B T_{\text{CMB}}} - e^{hv_{ul}/k_B T_{\text{ex}}}} \int T_B dv. \quad (\text{A11})$$

The total column can be derived from the column in the upper state using the partition function and the Boltzmann distribution

$$n_{\text{tot}} = \sum_{J=0}^{\infty} n_J = n_0 \sum_{J=0}^{\infty} (2J+1) \exp\left(-\frac{J(J+1)B_e h}{k_B T_{\text{ex}}}\right). \quad (\text{A12})$$

(A13)

This equation is frequently approximated using an integral (e.g. Cabrit & Bertout 1990), but a more accurate numerical solution using up to thousands of rotational states is easily computed

$$n_J = \left[ \sum_{j=0}^{j=j_{\text{max}}} (2j+1) \exp\left(-\frac{j(j+1)B_e h}{k_B T_{\text{ex}}}\right) \right]^{-1} (2J+1) \exp\left(-\frac{J(J+1)B_e h}{k_B T_{\text{ex}}}\right). \quad (\text{A14})$$

The effects of using the approximation and the full numerical solution are shown in Fig. A1.

The CO 3–2 transition is also less likely to be in LTE than the 1–0 transition. The critical density ( $n_{\text{cr}} \equiv A_{ul}/C_{ul}$ ) of  $^{12}\text{CO}$  3–2 is 27 times higher than that for 1–0. We have run RADEX (van der Tak et al. 2007) LVG models of CO to examine the impact of sub-thermal excitation on column derivation. The results of the RADEX models are shown in Fig. A2. They illustrate that, while it is quite safe to assume the CO 1–0 transition is in LTE in most circumstances, a similar assumption is probably invalid for the CO 3–2 transition in typical molecular cloud environments.

## SUPPORTING INFORMATION

Additional Supporting Information may be found in the online version of this article:

**Figures 27–78.** Position–velocity diagrams, contour overlays on infrared images and integrated spectra for all of the outflows identified in the survey.

Please note: Wiley-Blackwell are not responsible for the content or functionality of any supporting materials supplied by the authors. Any queries (other than missing material) should be directed to the corresponding author for the article.

This paper has been typeset from a TeX/LaTeX file prepared by the author.

## QUERIES

Journal: MNR  
Paper: mnr\_19279

Dear Author

During the copy-editing of your paper, the following queries arose. Please respond to these by marking up your proofs with the necessary changes/additions. Please write your answers on the query sheet if there is insufficient space on the page proofs. Please write clearly and follow the conventions shown on the corrections sheet. If returning the proof by fax do not write too close to the paper's edge. Please remember that illegible mark-ups may delay publication.

Query Reference	Query	Remarks
Q1	Author: If your paper has figures that you wish to be in colour in the printed journal and you have not yet returned your colour work agreement form, please do so urgently, as your paper cannot be published until the form has been received. Please notify us (via your proof corrections or an email to <a href="mailto:mnr@wiley.com">mnr@wiley.com</a> ) to expect the form. It can be downloaded from <a href="http://www.blackwellpublishing.com/pdf/mnr_form.pdf">http://www.blackwellpublishing.com/pdf/mnr_form.pdf</a> . Important: to comply with UK Payment Card Industry Data Security Standard (PCI DSS) legal requirements, all forms must be received as original signed hardcopies sent by post – electronic or faxed copies cannot be accepted. Please return your form to MNRAS, Wiley-Blackwell, John Wiley & Sons, 101 George Street, Edinburgh, EH2 3ES, UK.	The printed journal does not need to be in color.
Q2	Author: To check that we have your surnames correctly identified and tagged (e.g. for indexing), we have coloured green the names that we have assumed are surnames. If any of these are wrong, please let us know so that we can amend the tagging.	The surnames are correct
Q3	Author: If you refer to any data bases in your paper, please note the journal policy for properly crediting those responsible for compiling the data base. Rather than citing only a URL, if at all possible please also cite a reference (and include it in the reference list), or if a reference is not available then the names of those who compiled the data base. Note that some data bases do provide guidelines on how they should be cited – please check for these and follow them in your paper where appropriate.	To the best of our knowledge, this has been done wherever possible. SIMBAD, though, does not have a paper reference, only a URL.
Q4	Author: Please check, the spelled out form of the acronym 'HARP' is not given.	The acronym is also commonly accepted as the instrument name; it (probably) does not need to be spelled out. The acronym stands for "Heterodyne Array Receiver Program", but I believe the instrument itself is just "HARP"

Query Reference	Query	Remarks
Q5	Author: The MNRAS list of approved key words has been revised and updated. The new list is appended to these proofs. If you had previously selected key words from the old list, please now check them carefully against the new list in case they need to be changed, or there are new ones that you would like to add. If you had not previously selected key words from the MNRAS approved list, please now choose up to six from the new list.	The keywords are acceptable as listed
Q6	Author: Please note that it is journal style to refer to 'our' Galaxy with a capital 'G' and to other galaxies with a lower-case 'g'. Please check that all the notations in this paper are correct.	At the bottom-right of Page 1, outer galaxy should be outer Galaxy. In section 3.2, galactic plane -> Galactic plane. In Figure 1 caption, galactic longitude -> Galactic longitude.
Q7	Author: Please check the spelled out form of the acronym 'OB' is not given.	OB is a classification system, not an acronym.
Q8	Author: Please check the figures in the PDF proof carefully	OK except Fig 2. (see note there)
Q9	Author: Please check, the spelled out form of the acronym ' DRAO CGPS' is not given.	DRAO = Dominion Radio Astronomy Observatory CGPS = Canadian Galactic Plane Survey
Q10	Author: Please check, the spelled out form of the acronym 'DSS R' is not given.	DSS = Digitized Sky Survey [R is a band name]
Q11	Author: Please check, the spelled out form of the acronym 'SEQUOIA' is not given.	SEQUOIA is an instrument name and can be left as-is
Q12	Author: The short title of a paper must not exceed 45 characters in length (including spaces). Please check the suitability of the suggested short title or provide another alternative.	Prefer "CO 3-2 Observations of W5"
Q13	Author: Please check, the spelled out form of the acronym 'SIMBAD' is not given.	SIMBAD is a name; they seem to prefer all caps
Q14	Author: According to the journal style, year-month-date pattern is to be followed. Please check if the edit in the dates in the sentence 'Additional...' retains the intended meaning.	2008 should precede August in the sentence (all dates in the sentence are 2008)
Q15	Author: Please check, the spelled out form of the acronym 'SIS' is not given.	SIS = superconductor-insulator-superconductor, but is rarely spelled out in the literature; I think it should be left as is. ACSIS is the name of the backend system
Q16	Author: Please note that computer software/programming languages must be styled in SMALL CAPITAL LETTERS, according to journal style. Please check and correct this paper accordingly.	
Q17	Author: Please check, the spelled out form of the acronym 'BGPS' is not given.	The sentence containing BGPS should be removed; it was left in as an oversight.
Q18	Author: Please check if the edit from ' $\theta_B = 50'$ (0.48 pc)' to ' $\theta_B = 50.0$ arcsec (0.48 pc)' retains the intended meaning.	please change "50.0 arcsec" to "50 arcsec"

Query Reference	Query	Remarks
Q19	Author: Please check, the spelled out form of the acronyms 'IRAC' and 'MIPS' are not given.	these are both instrument names
Q20	Author: Please provide the spelled out form of the acronym 'KS'.	KS = Kolmogorov-Smirnov
Q21	Author: Please check, the expression 'to inform our expectations' seems unclear.	change to "to predict their detectability"
Q22	Author: All Tables must be cited, and in numerical order, in the text. Table 1 in this paper is cited out of order; please change the text so that journal style is adhered to. Otherwise the tables themselves will need to be renumbered and repositioned accordingly.	Unfortunately, I don't think it is possible to include a reference to Table 1 any earlier or Table 2 any later; it is therefore more straightforward to renumber and reorder the tables.
Q23	Author: Please check, the spelled out form of the acronym 'COMPLETE' is not given.	COMPLETE is a survey name; it is not typically spelled out when cited
Q24	Author: Please check, no link for the footnotes are given in the table body. If they are general statements without any footnote links then we need to insert the term <i>Note</i> . at the beginning and make them run-on.	These are general statements and should be preceded by "Note:"
Q25	Author: Please check that they have been set OK.	the facility names look fine
Q26	Author: Please provide its location.	"Volume I: The Northern Sky ASP Monograph Publications" (the ADS page: <a href="http://adsabs.harvard.edu/abs/2008hsf1.book..308B">http://adsabs.harvard.edu/abs/2008hsf1.book..308B</a> )
Q27	Author: List all authors if eight or fewer.	>8 authors
Q28	Author: Please provide the name of the publisher and its location.	<a href="http://adsabs.harvard.edu/abs/2002ASPC..267..347B">http://adsabs.harvard.edu/abs/2002ASPC..267..347B</a> ASP Conference Proceedings, Vol. 267
Q29	Author: Please check either volume or page number is missing.	vol 408, pg 1516-1539 [the ADS bibtex information was changed]
Q30	Author: Not cited in text.	Please remove the citation
Q31	Author: List all authors if eight or fewer.	>8 authors
Q32	Author: List all authors if eight or fewer.	>8 authors
Q33	Author: List all authors if eight or fewer.	>8 authors
Q34	Author: Please check the name of the journal is not given. Also check if the page number is OK.	\bibitem[Hatchell & Dunham(2009)]{2009A&A...502..139H} Hatchell, J., \& Dunham, M.~M.~I. 2009, \aap, 502, 139

Query Reference	Query	Remarks
Q35	Author: Please check, can we delete the expression 'is always...' appearing after the reference. Only journal name, volume and page numbers are allowed as per the style requirement.	yes; I have no idea how that note got there
Q36	Author: List all authors if eight or fewer and update reference.	>8; \bibitem[Reid et al.(2009)]{2009ApJ...700..137R} Reid, M.~J., et al.\ 2009, \apj, 700, 137
Q37	Author: List all authors if eight or fewer.	>8
Q38	Author: Please provide the location of the publisher.	Springer-Verlag, Berlin, Germany, 2009.,
Q39	Author: when used to mean 'exponential', the letter 'e' in an equation must always be written in roman (i.e. 'e' rather than 'e'). The same applies to 'i' when used to mean 'the square root of -1'. Please check all the notation throughout the text carefully.	those changes should be made
Q40	Author: Please check equation (A13) is not given. Either we have to insert an equation for (A13) or we have to delete the number and renumber the following equation.	There is no equation A13; that line should be removed and A14 should be numbered A13. The "align" environment generated an extra eqn number
Q41	Author: Please check, the spelled out form of the acronym 'RADEX' is not given. Also check that if 'ul' given as subscript refers to a word (as subscript cr stands for 'critical') then we have to give it in roman. Please suggest.	RADEX is a code name, not an acronym. 'ul' refers to 'upper-lower' but is not directly an acronym, just a convenient choice of variable names; it should be left italicized.

# List of astronomical key words

## (updated 2009 December)

This list is common to *Monthly Notices of the Royal Astronomical Society*, *Astronomy and Astrophysics*, and *The Astrophysical Journal*. In order to ease the search, the key words are subdivided into broad categories. No more than six subcategories altogether should be listed for a paper.

The subcategories in boldface containing the word ‘individual’ are intended for use with specific astronomical objects; these should never be used alone, but always in combination with the most common names for the astronomical objects in question. Note that each object counts as one subcategory within the allowed limit of six.

The parts of the key words in italics are for reference only and should be omitted when the key words are entered on the manuscript.

### General

editorials, notices  
errata, addenda  
extraterrestrial intelligence  
history and philosophy of astronomy  
miscellaneous  
obituaries, biographies  
publications, bibliography  
sociology of astronomy  
standards

### Physical data and processes

acceleration of particles  
accretion, accretion discs  
asteroseismology  
astrobiology  
astrochemistry  
astroparticle physics  
atomic data  
atomic processes  
black hole physics  
chaos  
conduction  
convection  
dense matter  
diffusion  
dynamo  
elementary particles  
equation of state  
gravitation  
gravitational lensing: strong  
gravitational lensing: weak  
gravitational lensing: micro  
gravitational waves  
hydrodynamics  
instabilities  
line: formation  
line: identification

line: profiles  
magnetic fields  
magnetic reconnection  
(*magnetohydrodynamics*) MHD  
masers  
molecular data  
molecular processes  
neutrinos  
nuclear reactions, nucleosynthesis, abundances  
opacity  
plasmas  
polarization  
radiation mechanisms: general  
radiation mechanisms: non-thermal  
radiation mechanisms: thermal  
radiative transfer  
relativistic processes  
scattering  
shock waves  
turbulence  
waves

### Astronomical instrumentation, methods and techniques

atmospheric effects  
balloons  
instrumentation: adaptive optics  
instrumentation: detectors  
instrumentation: high angular resolution  
instrumentation: interferometers  
instrumentation: miscellaneous  
instrumentation: photometers  
instrumentation: polarimeters  
instrumentation: spectrographs  
light pollution  
methods: analytical  
methods: data analysis  
methods: laboratory  
methods: miscellaneous  
methods: numerical  
methods: observational  
methods: statistical  
site testing  
space vehicles  
space vehicles: instruments  
techniques: high angular resolution  
techniques: image processing  
techniques: imaging spectroscopy  
techniques: interferometric  
techniques: miscellaneous  
techniques: photometric  
techniques: polarimetric  
techniques: radar astronomy  
techniques: radial velocities

techniques: spectroscopic  
telescopes

### Astronomical data bases

astronomical data bases: miscellaneous  
atlases  
catalogues  
surveys  
virtual observatory tools

### Astrometry and celestial mechanics

astrometry  
celestial mechanics  
eclipses  
ephemerides  
occultations  
parallaxes  
proper motions  
reference systems  
time

### The Sun

Sun: abundances  
Sun: activity  
Sun: atmosphere  
Sun: chromosphere  
Sun: corona  
Sun: coronal mass ejections (CMEs)  
Sun: dynamo  
Sun: evolution  
Sun: faculae, plages  
Sun: filaments, prominences  
Sun: flares  
Sun: fundamental parameters  
Sun: general  
Sun: granulation  
Sun: helioseismology  
Sun: heliosphere  
Sun: infrared  
Sun: interior  
Sun: magnetic topology  
Sun: oscillations  
Sun: particle emission  
Sun: photosphere  
Sun: radio radiation  
Sun: rotation  
(*Sun:*) solar-terrestrial relations  
(*Sun:*) solar wind  
(*Sun:*) sunspots  
Sun: surface magnetism  
Sun: transition region  
Sun: UV radiation  
Sun: X-rays, gamma-rays

### Planetary systems

comets: general  
**comets: individual: ...**  
Earth

interplanetary medium

Kuiper belt: general

**Kuiper belt objects: individual: ...**

meteorites, meteors, meteoroids

minor planets, asteroids: general

**minor planets, asteroids: individual: ...**

Moon

Oort Cloud

planets and satellites: atmospheres

planets and satellites: aurorae

planets and satellites: composition

planets and satellites: detection

planets and satellites: dynamical evolution and stability

planets and satellites: formation

planets and satellites: fundamental parameters

planets and satellites: general

**planets and satellites: individual: ...**

planets and satellites: interiors

planets and satellites: magnetic fields

planets and satellites: physical evolution

planets and satellites: rings

planets and satellites: surfaces

planets and satellites: tectonics

planet-disc interactions

planet-star interactions

protoplanetary discs

zodiacal dust

### Stars

stars: abundances

stars: activity

stars: AGB and post-AGB

stars: atmospheres

(stars:) binaries (*including multiple*): close

(stars:) binaries: eclipsing

(stars:) binaries: general

(stars:) binaries: spectroscopic

(stars:) binaries: symbiotic

(stars:) binaries: visual

(stars:) blue stragglers

(stars:) brown dwarfs

stars: carbon

stars: chemically peculiar

stars: chromospheres

(stars:) circumstellar matter

stars: coronae

stars: distances

stars: dwarf novae

stars: early-type

stars: emission-line, Be

stars: evolution

stars: flare

stars: formation

stars: fundamental parameters

(stars:) gamma-ray burst: general

(stars:) **gamma-ray burst: individual: ...**

stars: general

(stars:) Hertzsprung–Russell and colour-magnitude diagrams

stars: horizontal branch

stars: imaging

**stars: individual: ...**

stars: interiors  
stars: kinematics and dynamics  
stars: late-type  
stars: low-mass  
stars: luminosity function, mass function  
stars: magnetars  
stars: magnetic field  
stars: massive  
stars: mass-loss  
stars: neutron  
(stars:) novae, cataclysmic variables  
stars: oscillations (*including pulsations*)  
stars: peculiar (*except chemically peculiar*)  
(stars:) planetary systems  
stars: Population II  
stars: Population III  
stars: pre-main-sequence  
stars: protostars  
(stars:) pulsars: general  
(stars:) **pulsars: individual: ...**  
stars: rotation  
stars: solar-type  
(stars:) starspots  
stars: statistics  
(stars:) subdwarfs  
(stars:) supergiants  
(stars:) supernovae: general  
(stars:) **supernovae: individual: ...**  
stars: variables: Cepheids  
stars: variables:  $\delta$  Scuti  
stars: variables: general  
stars: variables: RR Lyrae  
stars: variables: S Doradus  
stars: variables: T Tauri, Herbig Ae/Be  
(stars:) white dwarfs  
stars: winds, outflows  
stars: Wolf-Rayet

**Interstellar medium (ISM), nebulae**  
ISM: abundances  
ISM: atoms  
ISM: bubbles  
ISM: clouds  
(ISM:) cosmic rays  
(ISM:) dust, extinction  
ISM: evolution  
ISM: general  
(ISM:) H II regions  
(ISM:) Herbig-Haro objects  
**ISM: individual objects: ...**  
(*except planetary nebulae*)  
ISM: jets and outflows  
ISM: kinematics and dynamics  
ISM: lines and bands  
ISM: magnetic fields  
ISM: molecules  
(ISM:) planetary nebulae: general  
(ISM:) **planetary nebulae: individual: ...**  
(ISM:) photodissociation region (PDR)  
ISM: structure  
ISM: supernova remnants

## The Galaxy

Galaxy: abundances  
Galaxy: bulge  
Galaxy: centre  
Galaxy: disc  
Galaxy: evolution  
Galaxy: formation  
Galaxy: fundamental parameters  
Galaxy: general  
(Galaxy:) globular clusters: general  
(Galaxy:) **globular clusters: individual: ...**  
Galaxy: halo  
Galaxy: kinematics and dynamics  
(Galaxy:) local interstellar matter  
Galaxy: nucleus  
(Galaxy:) open clusters and associations: general  
(Galaxy:) **open clusters and associations: individual: ...**  
(Galaxy:) solar neighbourhood  
Galaxy: stellar content  
Galaxy: structure

## Galaxies

galaxies: abundances  
galaxies: active  
(galaxies:) BL Lacertae objects: general  
(galaxies:) **BL Lacertae objects: individual: ...**  
galaxies: bulges  
galaxies: clusters: general  
**galaxies: clusters: individual: ...**  
galaxies: clusters: intracluster medium  
galaxies: distances and redshifts  
galaxies: dwarf  
galaxies: elliptical and lenticular, cD  
galaxies: evolution  
galaxies: formation  
galaxies: fundamental parameters  
galaxies: general  
galaxies: groups: general  
**galaxies: groups: individual: ...**  
galaxies: haloes  
galaxies: high-redshift  
**galaxies: individual: ...**  
galaxies: interactions  
(galaxies:) intergalactic medium  
galaxies: irregular  
galaxies: ISM  
galaxies: jets  
galaxies: kinematics and dynamics  
(galaxies:) Local Group  
galaxies: luminosity function, mass function  
(galaxies:) Magellanic Clouds  
galaxies: magnetic fields  
galaxies: nuclei  
galaxies: peculiar  
galaxies: photometry  
(galaxies:) quasars: absorption lines  
(galaxies:) quasars: emission lines  
(galaxies:) quasars: general  
(galaxies:) **quasars: individual: ...**  
galaxies: Seyfert

galaxies: spiral  
galaxies: starburst  
galaxies: star clusters: general  
**galaxies: star clusters: individual: ...**  
galaxies: star formation  
galaxies: statistics  
galaxies: stellar content  
galaxies: structure

infrared: galaxies  
infrared: general  
infrared: ISM  
infrared: planetary systems  
infrared: stars  
radio continuum: galaxies  
radio continuum: general  
radio continuum: ISM  
radio continuum: planetary systems  
radio continuum: stars  
radio lines: galaxies  
radio lines: general  
radio lines: ISM  
radio lines: planetary systems  
radio lines: stars  
submillimetre: diffuse background  
submillimetre: galaxies  
submillimetre: general  
submillimetre: ISM  
submillimetre: planetary systems  
submillimetre: stars  
ultraviolet: galaxies  
ultraviolet: general  
ultraviolet: ISM  
ultraviolet: planetary systems  
ultraviolet: stars  
X-rays: binaries  
X-rays: bursts  
X-rays: diffuse background  
X-rays: galaxies  
X-rays: galaxies: clusters  
X-rays: general  
**X-rays: individual: ...**  
X-rays: ISM  
X-rays: stars

## Cosmology

(*cosmology*:) cosmic background radiation  
(*cosmology*:) cosmological parameters  
cosmology: miscellaneous  
cosmology: observations  
cosmology: theory  
(*cosmology*:) dark ages, reionization, first stars  
(*cosmology*:) dark energy  
(*cosmology*:) dark matter  
(*cosmology*:) diffuse radiation  
(*cosmology*:) distance scale  
(*cosmology*:) early Universe  
(*cosmology*:) inflation  
(*cosmology*:) large-scale structure of Universe  
(*cosmology*:) primordial nucleosynthesis

## Resolved and unresolved sources as a function of wavelength

gamma-rays: diffuse background  
gamma-rays: galaxies  
gamma-rays: galaxies: clusters  
gamma-rays: general  
gamma-rays: ISM  
gamma-rays: stars  
infrared: diffuse background

# MARKED PROOF

## Please correct and return this set

Please use the proof correction marks shown below for all alterations and corrections. If you wish to return your proof by fax you should ensure that all amendments are written clearly in dark ink and are made well within the page margins.

<b>Instruction to printer</b>	<b>Textual mark</b>	<b>Marginal mark</b>
Leave unchanged	... under matter to remain	(J)
Insert in text the matter indicated in the margin	Λ	New matter followed by Λ or Λ②
Delete	/ through single character, rule or underline ——— through all characters to be deleted	⊖ or ⊖②
Substitute character or substitute part of one or more word(s)	/ through letter or ——— through characters	new character / or new characters /
Change to italics	— under matter to be changed	↖
Change to capitals	≡ under matter to be changed	≡
Change to small capitals	== under matter to be changed	==
Change to bold type	~ under matter to be changed	~
Change to bold italic	~~ under matter to be changed	~~
Change to lower case	Encircle matter to be changed	≡
Change italic to upright type	(As above)	⊕
Change bold to non-bold type	(As above)	⊕
Insert 'superior' character	/ through character or Λ where required	Y or X under character e.g. Y or X
Insert 'inferior' character	(As above)	Λ over character e.g. Λ
Insert full stop	(As above)	◎
Insert comma	(As above)	,
Insert single quotation marks	(As above)	Y or X and/or Y or X
Insert double quotation marks	(As above)	Y or X and/or Y or X
Insert hyphen	(As above)	H
Start new paragraph	└	└
No new paragraph	≈	≈
Transpose	└	└
Close up	linking ( ) characters	( )
Insert or substitute space between characters or words	/ through character or Λ where required	Y
Reduce space between characters or words	between characters or words affected	↑